INCREASING ELECTRIC MACHINE POWER DENSITY WITH A NEW END-WINDING COOLING SYSTEM

A Dissertation
Presented to
The Academic Faculty

by

Sebastien Sequeira

In Partial Fulfillment
of the Requirements for the Degree
Master of Science in the
G. W. Woodruff School of Mechanical Engineering

Georgia Institute of Technology
May 2021

INCREASING ELECTRIC MACHINE POWER DENSITY WITH A NEW END-WINDING COOLING SYSTEM

Approved by:

Dr. Yogendra Joshi, Co-Advisor (ME)
G. W. Woodruff School of Mechanical Engineering
Georgia Institute of Technology

Dr. Satish Kumar, Co-Advisor (ME)
G. W. Woodruff School of Mechanical Engineering
Georgia Institute of Technology

Dr. Sreekant Narumanchi (ME)
National Renewable Energy Laboratory

Date Approved: [April 22, 2021]

To my partner, my sister, and my parents

ACKNOWLEDGEMENTS

TABLE OF CONTENTS

LIST OF TABLES

LIST OF FIGURES

LIST OF SYMBOLS AND ABBREVIATIONS

AC   Alternative Current

CFD   Computational Fluid Dynamics

DAQ   Data Acquisition

DC   Direct Current

EV   Electric Vehicle

FDM   Fused Deposition Modeling

FEA   Finite Element Analysis

HTC   Heat transfer coefficients

IPM   Internal Permanent Magnet

LPTN   Lumped Parameter Thermal Network

NASA   National Aeronautics and Space Administration

NREL   National Renewable Energy Laboratory

RMS   Root Mean Square

WEG   Water Ethylene Glycol

SUMMARY

One of the key challenges for the electric vehicle industry is to develop high-power-density electric motors. Achieving higher power density requires efficient heat removal from inside the motor. For high performance electric motors, water-jacket cooling systems are usually used to remove heat coming from the windings and the laminations. However, this limits the maximum power density as the coolant is far away from the slots. Moreover, this radial heat transfer through the laminations causes the end-windings to be the main hot-spot of the motor. Today, several solutions have been developed to have a direct cooling of these end-windings and further increase the power density of the motor. The first solution are fan blades placed on top of the rotor. This solution based on forced air convection only is limited by a low maximum heat transfer coefficient (HTC). The next method which has gained interest in the automotive industry is oil spray or jet impingement directly onto the end-windings. This provides much higher HTC. However, the coolant in contact with end-windings must be dielectric (oil is typically used) which results in an additional cooling loop for the vehicle. The last one is high thermal conductivity potting material which enhance the heat transfer from the end-winding to the housing. However, this solution still faces limitation in terms of mass production feasibility. Thus, this thesis proposed the investigation of a new type of cooling system based on end-winding channels. This new solution allows for high HTC using the same cooling loop as for the water-jacket. Besides, the design of these channels has been envisioned for an easy integration in the end-windings with the goal of mass production capability.

CHAPTER 1.   INTRODUCTION

1.1   Motivation

Over the last decade, the number of electric vehicles (EVs) on the road has increased significantly [1]. However, one of the main limiters to EV adoption is the range which is currently lower than conventional internal combustion engine vehicles. One solution to improve this range is to increase the power density of the electric motors used in the EVs. In this regard, an electric motor power density target of 50 kW/L by 2025 was set by U.S. DRIVE consortium, part of the U.S. Department of Energy [2]. For a long time, electric motor designers were focused on electromagnetic optimization of electric motors as the electric machines were mostly used for industrial (non-mobile) applications and did not require high power densities. However, the application of electric motors to EVs reveals higher concerns on the thermal management of electric machines. Consequently, the thermal constraints quickly become the main limitation to the higher power density objectives for electric motors [3].

The thermal constraints in electric machines are related to the temperature limitation of specific components. For internal permanent magnet (IPM) motors, high temperatures can cause the demagnetization of the magnets in the rotor [4] which can lead to a significant drop in motor performance of more than 50% [5]. High temperatures can also cause degradation of the winding insulation, and the insulation lifetime is typically divided by 2 for a 10°C increase in the average operating temperature of the motor [6]. Besides, the windings are particularly critical as they often represent the hot spot of the machine [7, 8].

Higher power densities imply higher temperatures of the motor for the same type of cooling system. Therefore, conventional cooling systems, like fins on the housing of totally enclosed non ventilated motors using natural convection [9], are typically not enough to cool high power density machines. Reaching the higher power densities requires the heat extraction from the heat sources of the motor, like the windings, to be much more efficient than natural convection. The use of forced air convection using internal or external fans can lead to better cooling performance of the motor. But this type of cooling system is often not enough to match the motor power density objectives for EVs. As a result, liquid cooling of electric machines is now generally used. A common liquid cooling system is the water-jacket [10, 11]. In this system, the coolant is flowing through channels around the stator, absorbing the heat from the windings. The heat transfer coefficient of the water-jacket is already much better than the conventional fan cooled machine. The value of this heat transfer coefficient can be higher than 3000 $W.m^{-2}.K^{-1}$ for 10 L/min flow rates [10]. However, the thermal resistance of the path from the winding to the coolant is limiting the cooling performance of the water-jacket [12, 13].

Current research on new motor cooling approaches is focused on direct cooling methods. Direct cooling methods consist in having the heat exchanger directly in contact with the windings or very close to the windings. This considerably reduces the thermal resistance between the coolant and the windings. Several concepts and prototypes of direct cooling systems were developed for the slot-winding regions. In [14, 15], thin ducts with internal pin fins are directly inserted inside the slots. Coolant is flowing through this heat exchanger, absorbing heat from the windings. Another approach using simple ducts without pin fins is presented in [16]. These solutions show very good performance in terms

2

of achieved power density. However, the fabrication of these ducts - especially for the ducts with pin fins - can be expensive and having an automated process to insert these heat exchangers inside the slots for mass production would probably be a significant challenge. Moreover, these slot-winding cooling solutions are not applied to the end-windings which represent the highest temperatures in the complete windings as shown in [8] or [10], hence the need for direct cooling method of the end-windings.

One of the currently adopted end-winding direct cooling methods is oil spray cooling or jet impingement. Oil is directly sprayed onto the end-windings absorbing heat from this region very efficiently. The obtained heat transfer coefficient for this cooling system can be as high as that of the water-jacket but without the constraint of the thermal resistance between the coolant and the winding, as the oil is in direct contact with the wires [17, 18]. However, this spray nozzle could face blockage issues [19] and further lead to significant reduced performance of the cooling system. Moreover, even though the oil used for this solution is generally the existing transmission fluid, an additional pump is required for the end-windings which increases the complexity of the complete powertrain system. Another approach for end-winding cooling consists in using potting material covering the end-windings as presented in [20, 21]. This potting material is generally a highly conductive compound which is poured in the end-winding and cures in place after a few hours. The temperature decrease of the end-windings is significant [20] which makes this solution very interesting. However, this potting material is an expensive solution considering the amount of material require for a complete potting of the end-windings. Moreover, vibrations of the motor can cause this highly conductive compound to crack. Eventually, the potting process generally needs to be under vacuum to expect good cooling performances. At ambient

pressure, a lot of air bubbles can be stuck inside the potting material because of its high viscosity.

A new approach using a tube directly inserted inside the end-windings allowed to achieve similar cooling performance compared to oil spray cooling or potting material methods [19]. The authors were able to achieve a 25% temperature reduction when using this end-winding tube and a water-jacket compared to a solution with water-jacket only. The same coolant in water-jacket was flowing through this tube which means no additional cooling loop is needed, unlike for the oil spray cooling method. Moreover, it is a much cheaper solution than potting material. The cooling performance of this system was achieved through the use of a flexible silicone tube. As the coolant flow is increased, the tube is expending, increasing the contact area between the tube and the winding, and thus increasing the heat flow. However, the insertion process would be difficult to scale up for an integration in EVs. Indeed, the silicone tubes are very soft and can be scratched very easily which may lead to a low reliability automation process for mass production. Moreover, the authors had to increase the height of the end-windings to be able to insert this curved tube. Therefore, they were adding copper losses which would have not existed without this tube. Finally, this system is suitable for concentrated winding motor type (used in [19]) but for distributed winding types of motors which represent the majority of EV motors, it will be more difficult to insert this tube in compact overlaying end-turns.

As shown in the previous paragraphs, end-winding cooling of electric machine is a significant challenge especially in terms of cost and mass scale production. However, the different end-winding cooling solutions presented above show the significant benefit of having a direct end-winding cooling system in terms of temperature decrease. Decreasing

4

the temperature for the same electric power input means a better lifetime of the winding and permanent magnets. Besides, the volume and the mass of the motor can be reduced while having the same output power, further increasing the range of EVs and their efficiency.

1.2 Objectives

The first objective of this work is to design and test a new end-winding cooling system for electric motors which has a good cooling performance as oil spray or potting material cooling solutions. This new end-winding cooling system must be scalable for mass production, use the same coolant as the water-jacket to have a single cooling loop and be designed for distributed windings. The developed cooling system was designed based on the Nissan Leaf motor reference. The features of this motor are shown in Table 1 [22].

Table 1 – Nissan Leaf electric motor features.

Feature	Value
Maximum torque [$N.m$]	280
Maximum power [kW]	80
Top speed [rpm]	10,390
Weight [kg]	58
Volume [m^3]	0.019
Number of poles	8
Number of stator slots	48

The second objective is to model this new cooling system using an equivalent resistance network so that it can be integrated into a complete Lumped Parameter Thermal Network (LPTN) of the Nissan Leaf motor, and be further compared with other cooling systems. Before integrating the developed end-winding cooling system into the LPTN, we must ensure that the LTPN of the original motor is validated.

1.3   Thesis overview

This thesis is organized into three parts. In CHAPTER 2, a background on the thermal analysis of electric motors is presented. This chapter helps understand the origin of the different heat sources in an electric motor, as well as the different types of modeling that can be used to predict the temperatures in the motor. Particular attention is given to the LPTN model as we will develop our own LPTN of the Nissan Leaf motor in the next chapter.

In CHAPTER 3, the validation of the Nissan Leaf LPTN model is performed. The LPTN model temperature outputs are compared to experimental data and results from Finite Element Analysis (FEA) model. Once this LPTN model is validated, we can combine it with the equivalent thermal network of the developed end-winding cooling system.

In CHAPTER 4, the end-winding cooling system design and fabrication process is presented. The end-winding cooling system is tested on the Nissan Leaf stator. The test procedure and the results are shown and discussed. Finally, the end-winding cooling system model and its calibration with the LPTN model developed in CHAPTER 3, are presented.

CHAPTER 2.   BACKGROUND

In this chapter, the different elements of electric motor thermal analysis are presented. In the first section, the heat sources causing temperature rise in an electric motor are presented. The power losses associated with these heat sources are also developed. In the second section, we explain how numerical methods like FEA, or Computational Fluid Dynamics (CFD) can accurately predict the temperatures of the motor once the heat sources are known. In the last section, we developed an alternative model to FEA and CFD which allows for faster computation. This analytical model is a LPTN. An exhaustive presentation of the different LPTN components and their definition is given. This LPTN modelling approach will then be applied to our IPM motor model developed in CHAPTER 3.

2.1   Heat sources

The temperature rise in an electric machine is due to different power losses in the machine. There are different types of power losses inside a machine and the value of each of these losses depends on the machine operating point.

The first type of power losses are copper losses, denoted as P_c. They are a consequence of Joule's first law applied to the winding of the motor. They represent the highest losses in a motor. These copper losses are defined as:

$$P_c = n_{ph} \times R_{ph} \times \left(I_{ph}\right)^2 \tag{1}$$

Where: n_{ph} is the number of phases in the motor (commonly 3 phases for IPM motors in electric vehicles), R_{ph} is the resistance of one phase and I_{ph} is the RMS value of the current.

In addition to copper losses, we may have AC (Alternative Currents) losses in the windings due to induced eddy-currents in the wires. These AC losses generally arises from slot leakage field and are negligible in the end-winding region [23]. More detailed analysis of these AC losses is provided in [23-25].

The third type of power losses are the core losses P_{core} which occurs in the laminations of the motor. These losses are due to alternating magnetic flux density in the machine. The core losses are usually defined after C.P. Steinmetz's work, as the sum of two separate loss component: the hysteresis losses P_h and the eddy current losses P_e. The hysteresis losses are observed as the magnetizing force applied to the core is changing its direction. This change in magnetization direction occurs as the magnetic flux is alternating. The eddy current losses are observed when currents are induced in the core due to an alternating current, according to Faraday's law of induction. From Joule's law these eddy currents generate heat. The first definition of P_{core} is given by Steinmetz equation below:

$$P_{core} = P_h + P_e = C_h f B^x + C_e f^2 B^2 \tag{2}$$

Where f is the excitation frequency, x a constant, C_h and C_e are the hysteresis and eddy current loss coefficient respectively and B is the peak flux density.

The constant x depends on the type of material. C_h depends on the frequency f and the material. These coefficients are generally given by the manufacturer or need to be

8

derived from tables giving the total loss versus flux density [26]. The Steinmetz equation results were found to underpredict the total core losses and an additional term was added corresponding to the excess losses. The origin and properties of this excess term were developed by G. Bertotti in [27] leading to equation (3):

$$P_{core} = C_h f B^x + C_e f^2 B^2 + C_{ex} f^{1.5} B^{1.5} \tag{3}$$

Where C_{ex} is the excess loss coefficient depending on the material properties.

Other comprehensive models which demonstrate the variation of coefficients with the temperature [28] or frequency [26, 29] can be more accurate, but the Steinmetz and Bertotti equations remains the most common equations used for the computation of core losses in electric machines.

In addition, we have mechanical losses which are due to friction. These friction losses can come from the bearings of the machine and from the friction of air in the gap between the rotor and the stator. The losses due to friction in the air gap are often called windage losses.

In this thesis, all the reported experiments are performed with DC currents. Consequently, all losses arising from AC currents will not be considered. This includes core losses and AC losses in the windings. Moreover, we will focus on the stator. All losses due to the presence of the rotor will not be considered. Eventually, the only losses that will exist in our study will be the copper losses P_c.

2.2 Numerical methods

In order to predict the temperatures in the motor, different methods can be used. The numerical methods are based on FEA and CFD with conjugate heat transfer. The FEA method is especially used to solve for conductive heat transfer. The solid domain in the motor is divided into small elements where the general heat equation given in equation (4) is approximated using weak functions to come up with a linear system of equations. This allows to obtain an accurate temperature distribution in the solid parts of the motor even when very complex geometries are involved [30]. Moreover, the other advantage of the FEA method for thermal analysis is that it can be directly coupled to a FEA model solving for the magnetic flux density in the same region as the thermal FEA model. The coupled analysis has been extensively used in the literature [31-35].

$$\rho c_p \frac{\partial T}{\partial t} = \nabla \cdot k \nabla T + q_V \tag{4}$$

Where ρ is the mass density of the solid, c_p is the specific heat of the solid, k is the thermal conductivity of the solid and q_V is the volumetric heat source.

When using conductive models only with the FEA method, convective heat transfer at the interface between a solid and a fluid is often derived using Newton's law of cooling given in equation (5) combined with convection correlations to determine the heat transfer coefficient h. A heat Neumann boundary condition is typically applied at the interface with the fluid by fixing the value of T_f and h. These convection correlations are often based on dimensionless number relations. The more useful dimensionless number for the convection correlations used in electric machines are the Nusselt number, Reynolds number, Prandtl number, Grashof number and Taylor number [9, 36].

$$q = hA(T_S - T_f) \tag{5}$$

Where h is the heat transfer coefficient, A the heat transfer area, T_S the temperature of the solid at the interface, and T_f the temperature of the fluid. For an external flow we consider this temperature to be the temperature of the fluid far from the interface, and for an internal flow this temperature is the mean temperature of the fluid [37].

By using the conductive model only with FEA models, we must rely on these empirical correlations to include any convective heat transfer in the model. CFD models using conjugate heat transfer do not need these correlations, as both the solid and fluid domains are fully solved. The complete fluid domain is divided into elementary cells corresponding to a control volume when using the finite volume method. For each of these cells the continuity equation, momentum equation and energy equation are solved. This allows to derive the heat transfer coefficient at the interface between the fluid and the solid without having to use any convective correlations. Moreover, CFD models can be useful when the fluid flow path is very complex like in the end-winding region [38, 39]. Indeed, with complex geometries it can be difficult to know how to apply convective correlations to each surface to accurately predict the temperatures. CFD model can even be used for the complete motor if computational power is not an issue [10].

One of the main drawbacks of the CFD and FEA approaches are their computational time [40]. During the design process, having simulations which can takes hours to compute the temperatures at each element or cell in the machine can drastically reduce the number of different designs that can be studied. Consequently, analytical models, like LPTN, can be used when a high number of design iterations is required. Even though these LPTN

models use a nodal discretization of the different parts of the machine leading to a much coarser resolution than FEA or CFD models, they require much less computational effort [36, 41]. LPTN model analysis and validation have been demonstrated in several papers for both steady-state and transient conditions, and for different types of motors [7, 8, 11, 36, 41-45]. More recent work on LPTN models provides an even more spatially resolved discretization especially for the windings [19, 46]. Most of the LPTN models are still combined with a 2D FEA model in a plane perpendicular to the axial direction of the motor to predict the magnetic flux density distribution in the slice of the motor using a time-stepping method over one electrical period. This FEA model is then combined with an analytical model to account for end-winding inductance in the magnetic circuit [8, 36]. While thermal FEA models can often be replaced by LPTN as both of them need convective correlations to model a complete electric machine [47], CFD modeling is still used in addition to LPTN models when new cooling systems involving complex flow and complex geometry are implemented.

2.3   Lumped Parameter Thermal Network

LPTN is a nodal network where nodes represent the temperatures of the system. Node are connected to each other with resistances. The heat sources are represented as a power source. If a transient analysis is considered, additional capacitors are added to the circuit to account for the ρc_p term from equation (4) for each component of the system. The LPTN resistances can either represent a conductive, convective, or radiative heat transfer. The convective heat transfer between a solid and a cooling fluid can be modelled by a thermal resistance R_{conv} defined as:

$$R_{conv} = \frac{1}{hA} \qquad (6)$$

Where h is the heat transfer coefficient and A is the area of the interface between the solid and the fluid.

The convection correlations based on the Nusselt number mentioned previously for FEA models are generally used to compute the value of h especially for the end-winding region and the airgap between the rotor and the stator. Otherwise, h can be computed using a CFD model. This is particularly suitable when designing a new cooling system, which is the case for the end-winding channel cooling system presented in this thesis.

The general definition of the resistance modelling conduction heat transfer across a solid body of thickness L, cross-section area A, and thermal conductivity k is given by:

$$R_{cond} = \frac{L}{kA} \qquad (7)$$

In the LPTN, two types of volumes are used to represent the components of the electrical machine. The first one is a general rectangular prism and the second is general cylindrical component.

A schematic of the rectangular prism is represented in Figure 1. First, we consider that we have a total generated heat q_x inside the prism and that heat is flowing along the x direction only. In this case, R. Wrobel and P. H. Mellor have shown in [48] that this thermal problem can be represented by a simple thermal network with three resistances as shown

in Figure 2. The expression for the resistances R_{1x}, R_{2x} and R_{3x} derived in [48] are given in the equations below:

$$R_{1x} = R_{2x} = \frac{l_x}{2k_x A_x} \tag{8}$$

$$R_{3x} = \frac{-l_x}{6k_x A_x} \tag{9}$$

Where k_x is the material thermal conductivity in the x direction.
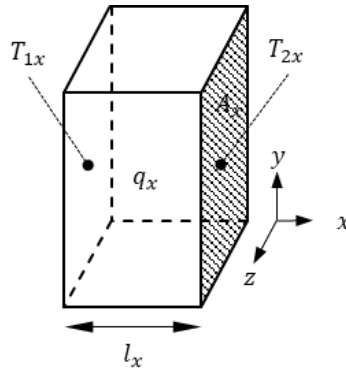
Figure 1 – Heat flow across the surface A_x of a rectangular prism of length l_x with internal heat generation q_x
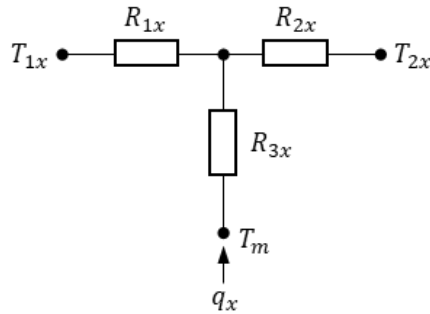
Figure 2 – Equivalent thermal network for one dimension heat flow in rectangular prism with internal heat generation q_x. T_m is the average temperature of the component.

If we now consider that we can have heat generation in x, y and z directions, we can use the thermal network from Figure 2 to create an equivalent thermal network for 3D heat transfer in the rectangular prism. This 3D equivalent thermal network is represented in Figure 3. This model assumes that the heat flows along each direction are independent which is a reasonable assumption for electrical machines. Considering non-independent heat flow would require having a full solution of the heat equation in 3D for any boundary condition … As we are in cartesian coordinates in a rectangular prism, the expression of (R_{1y}, R_{2y}, R_{3y}) and (R_{1z}, R_{2z}, R_{3z}) are the same as in equations (8) and (9). Besides, the thermal conductivities k_y and k_z along the y and z directions respectively can be different, which suggests that this model is ideal to represent anisotropic material like the windings [48].
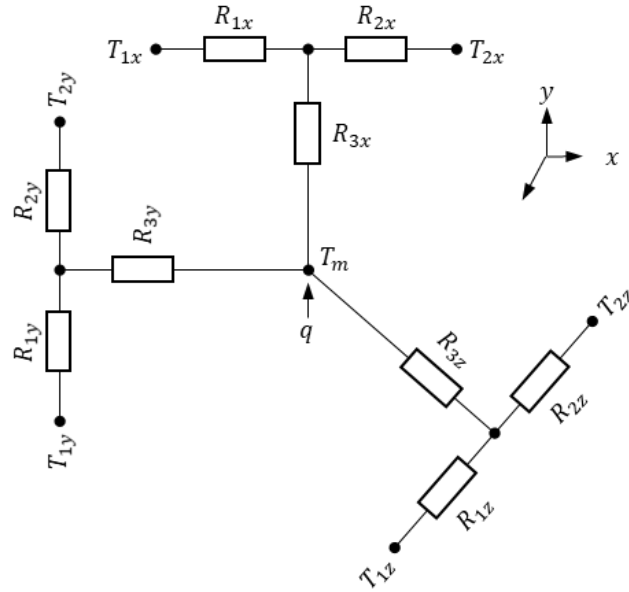
Figure 3 – Equivalent thermal network for 3D heat flow in a rectangular prism with a total internal heat generation q [48].

Some components have a simplified version of the complete thermal network from Figure 3. The liner region of the motor for example is a simple sheet with a low thickness (around 0.25 mm for the Nissan Leaf motor). As a result, for this component we can consider that the heat flow is along the normal to the sheet only. Moreover, there is no heat source in the liner. Accordingly, the liner equivalent network will just be a two-resistance network equivalent to that from Figure 2 without R_{3x} resistance as $q_x = 0$. However, the windings will need to have the full thermal network from Figure 3. In the LPTN software Motor-CAD® that we will be using in the next chapter to generate the LPTN of the Nissan Leaf motor, this full model is used for both the slot-windings and end-windings.

In an electrical machine, many components have a cylindrical shape like the stator core, the housing, or the shaft. We must consider the heat transfer in both the radial and axial directions, and account for any heat source component in case any losses generated are in this component. A general cylindrical component of the motor is shown in Figure 4 and is extracted from [36]. In this cylinder we consider that we have independent heat flow along the radial and axial direction. This assumption was proven the be a valid assumption based on experimental results comparison in [30, 48]. As the heat flow along each direction is assumed to be independent, an equivalent network of the general cylindrical component with heat generation can be defined as shown in Figure 5 [36]. This representation from [36] can be also found in [30].
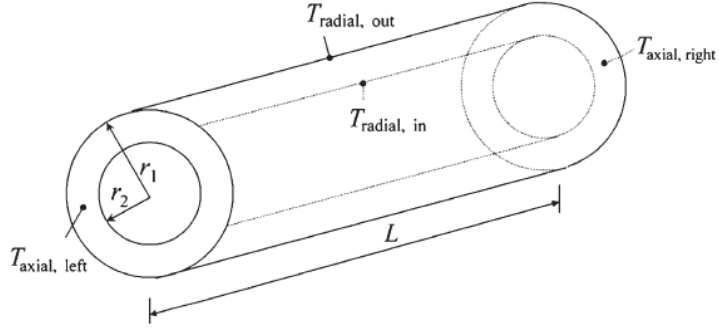
Figure 4 – General cylindrical component of length L, outer diameter r_1 and inner diameter r_2 [36].
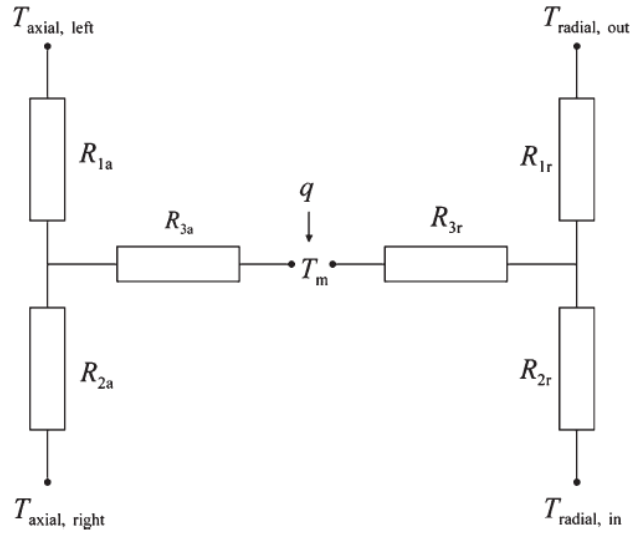
Figure 5 – Independent axial and radial thermal network for a general cylindrical component. T_m is the average temperature of the cylindrical component and q is the heat source of the cylindrical component [36].

The expression for each resistance in the thermal network in Figure 5 are given in the equations below:

$$R_{1a} = R_{2a} = \frac{L}{2\pi k_a (r_1^2 - r_2^2)} \tag{10}$$

$$R_{3a} = -\frac{L}{6\pi k_a (r_1^2 - r_2^2)} \tag{11}$$

$$R_{1r} = \frac{1}{4\pi k_r L}\left(1 - \frac{2r_2^2 \ln\left(\frac{r_1}{r_2}\right)}{r_1^2 - r_2^2}\right) \tag{12}$$

$$R_{2r} = \frac{1}{4\pi k_r L}\left(\frac{2r_1^2 \ln\left(\frac{r_1}{r_2}\right)}{r_1^2 - r_2^2} - 1\right) \tag{13}$$

$$R_{3r} = \frac{1}{8\pi k_r L(r_1^2 - r_2^2)}\left(\frac{4r_1^2 r_2^2 \ln\left(\frac{r_1}{r_2}\right)}{r_1^2 - r_2^2} - r_1^2 - r_2^2\right) \tag{14}$$

Where k_a and k_r are the thermal conductivity of the material along the axial and radial direction respectively.

The general thermal network for a hollow cylinder from Figure 5 can be adapted to the heat transfer scenario. For example, if the cylindrical component in the motor does not generate losses like the housing, its equivalent thermal network would be that from Figure 5 without R_{3a} and R_{3r} as $q = 0$. It is worth noticing that not tangential heat transfer is considered. Indeed, in the electric motor, all the parts which can be represented by a cylindrical component have a negligible heat flow along the tangential direction.

Finally, in case of a transient study we may have a capacitance connected to the T_m node equal to $\rho c_p V$ where V is the volume of the component. This applies to both the hollow cylinder and rectangular prism geometries.

CHAPTER 3.   VALIDATION OF AN IPM MOTOR LPTN

In this chapter, the LPTN model of the Nissan Leaf motor is developed. This LPTN will then be used in CHAPTER 4 to model the integration of the developed end-winding cooling system in this thesis. The main objective of the chapter is to validate this LPTN against the FEA model as well as experimental data.

As we are focused on the cooling of the end-winding, only the stator will be considered for the rest of this thesis. Previous work on LPTN validation [41, 42, 46] through comparison with experimental data was focused on analyzing individual temperature points. However, this is not enough information to understand how each component contributes to the temperature rise inside the stator. Here we propose a different approach by analyzing temperature profiles along three different paths of the motor, with particular attention to the end-windings region and the different contact interfaces in the stator as they will have a direct impact on the performance of the developed end-winding cooling system.

Each thermal parameter of our LPTN is clearly investigated, and the relations between the LPTN parameters and FEA parameters are given. Moreover, the sensitivity of the main thermal parameters is computed. The thermal parameters with the highest influence on the increase in motor temperatures were identified through this sensitivity analysis. We also explain how this influence is related to future motor cooling system requirements.

3.1   Experimental data and modeling approach

The Nissan Leaf Electric Motor from Nissan Motor Co. Ltd. is our reference for all geometric, material, and thermal parameters used in this chapter. The only active cooling system in the Nissan Leaf motor is an external water jacket composed of 3 channels in series made of aluminum. The water jacket coolant is Water-Ethylene Glycol (WEG).

The experimental results used in this study are taken from previous experiments in [49]. In these experiments, the windings were supplied with DC current (voltage of 1.4V and current of 165 amps) and the rotor was removed from the motor. The total heat generation from the 3 phases of the motor was 567 W. The only heat rejection system was the water-jacket. The latter was filled with WEG coolant at 50% volume of water. The flow rate was 10 L/min. Insulation was used to reduce natural convection from the external surfaces directly exposed to ambient air (end-windings, inner stator, housing). The boundary conditions of these experiments are shown in Figure 6.

Temperature were measured with K-type thermocouples [49]. The location of each thermocouple is shown in Figure 6 (black and white crosses). All temperature points in the cross-section plane, Figure 6, except the *Housing* temperature points, are measured in two other cross-section planes rotated by 120° and 240° with respect to the motor axial axis.

For this study, we consider that a temperature label can be the same for different thermocouples or temperatures by assuming stator symmetries. A set of temperature points having the same label means they should all have the same temperature value based on the assumed symmetries in the models defined thereafter. For instance, we assume that *End-windings Inside* temperature points have the same value for both rear and front end-windings. Similarly, we consider that the *Stator inner face* temperature points have the

same temperature along the axial length of the tooth. These assumptions are made to enable a consistent comparison between experimental data and modeling results.
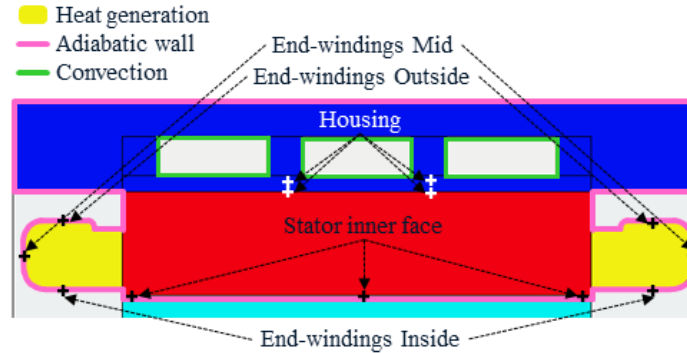
Figure 6 – Thermocouple locations on the Leaf motor stator and their associated labels, using Motor-CAD® environment. Heat generation and boundary conditions are shown as well.

By assuming these symmetries, we end up with only five different temperatures to be compared against the modeling results. In fact, inserting thermocouples inside the stator or the windings requires dismantling the laminations or the slot-windings, which would cause a different thermal behavior of the machine. This represents one of the main difficulties for model validation against experimental temperature values. However, in order to have a good validation of the LPTN model, we still need to know if the temperatures inside the stator and the slot-windings are consistent. Therefore, the LPTN temperature outputs are also compared to FEA modeling results of the complete stator. This FEA model is presented in the next section.

3.1.1   FEA model approach

We used the same motor geometry and boundary conditions in the FEA model as for the experiments. The same power loss input (567 W) was used and radiation and

convection to ambient air are neglected. Table 2 gives thermal conductivities for each material involved in the model, thermal contact conductance at each interface and the water-jacket thermal properties. Thermal conductivity and conductance are estimated from the data provided in [50-52].

Table 2 – Thermal conductivities along each direction of a cylindrical system and thermal contact conductance used for the FEA model along with water jacket thermal properties [49-52].

Thermal conductivity [$W.m^{-1}.K^{-1}$]			
	Radial	Tangential	Axial
Stator Laminations	21.9	21.9	1.77
Slot-Windings	0.99	0.99	292
End-Windings	0.76	202	101
Slot liner	0.18	0.18	0.18
Aluminum	167	167	167
Thermal contact conductance [$W.m^{-2}.K^{-1}$]			
Slot-Windings | Liner			1645
Liner | Laminations			556
Laminations | Housing			5555
Water-jacket cooling system			
Heat transfer coefficient [$W.m^{-2}.K^{-1}$]			1428
Flow rate [$L.min^{-1}$]			10.0
Coolant mean temperature [°C]			65

The water-jacket heat-transfer coefficient is derived from a CFD/HT simulation of the complete water-jacket channels in [49]. The coolant mean temperature value in the water-jacket is also taken from [49]. The tests in [14, 15] were conducted based on the Nissan Leaf motor parts. This makes the evaluation of the FEA model thermal parameters

more accurate than deducing these from a different motor. We must note that the values for Slot-Windings-to-Liner and Liner-to-Laminations thermal contact conductances are not exactly the same values as those provided in [49]. Indeed, NREL provided slightly different values which were not published yet. These values are preliminary results which require further confirmation.

Two pictures of the FEA model mesh are shown in Figure 7. The average mesh size was fixed at 2.7 mm. This choice relies on a mesh independence study. For this independence study, computing time and maximum temperature versus mesh size results were obtained (see Figure 8). Red labelled markers in Figure 8 correspond to the final average mesh size of the FEA model. With this final mesh size of 2.7 mm, the numerical results are accurate to within 0.4%.
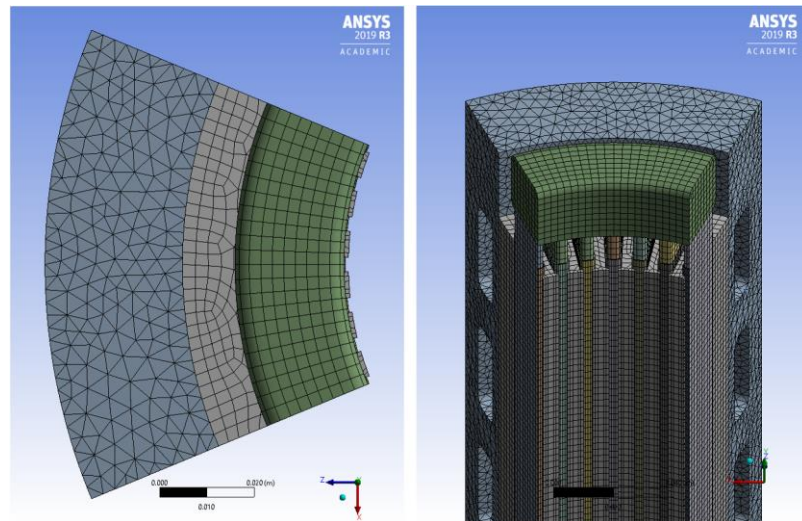
Figure 7 – Mesh of the FEA model (average size of 2.7 mm).
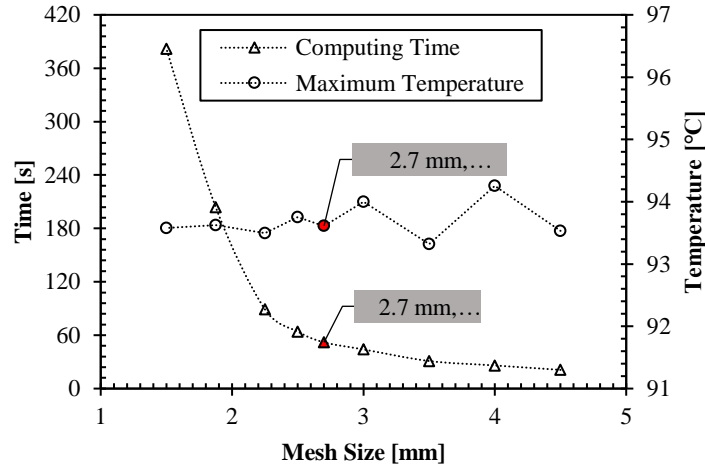
Figure 8 – Computing time and maximum temperature of the FEA model with respect to mesh size.

3.1.2 *Lumped Parameter Thermal Network model approach*

The LPTN model was created using Motor-CAD® software environment, where the electric motor geometry is designed first. All dimensions from the FEA model were kept for the LTPN model. Figure 9 shows cross-sectional views of the geometry. The radial and axial views are shown on the left and right respectively. A simplified version of the LPTN defined from this geometry is given in Figure 10. Each colored resistance accounts for the thermal conduction through a given part of the stator. The white resistances account for thermal contact resistance at the interface between two parts of the stator. Each node of the network represents a temperature and the sources of the circuit correspond to the copper losses generated inside the windings (567 W) as defined in CHAPTER 2. The LPTN main parameters are defined thereafter.
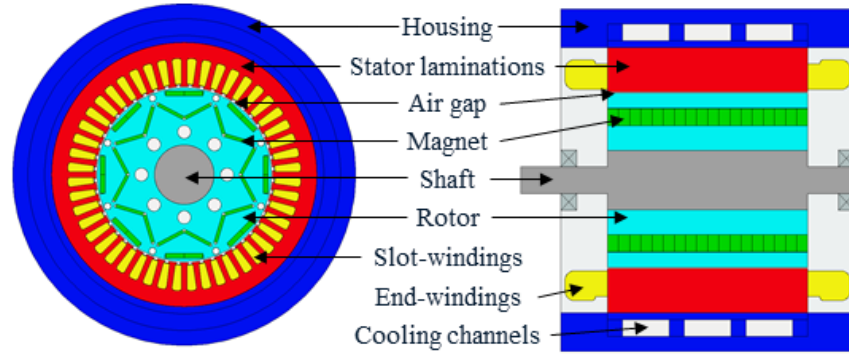
Figure 9 – Nissan Leaf motor geometry in Motor-CAD® environment: radial cross-sectional view on the left, axial cross-sectional view on the right.
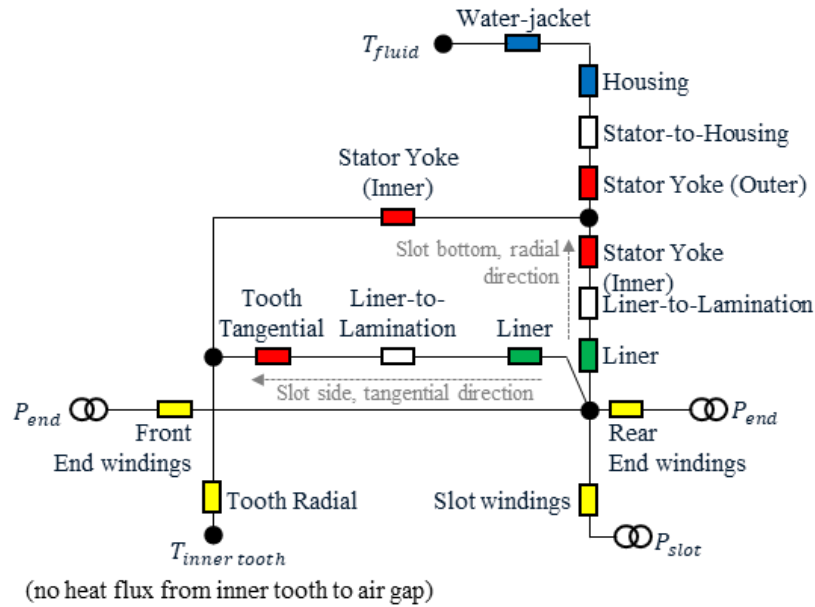
Figure 10 – Simplified representation of the stator LPTN model (based on Motor-CAD® schematic).

3.1.2.1 Power loss distribution

To be aligned with experimental results, the winding power losses are equal to the copper losses from DC currents in each phase of the stator. As we do not have AC currents in this study, we do not have any core losses or eddy current losses in the windings as defined in CHAPTER 2. As a result, the total power loss input P in the LPTN model is

equal to the total electric power input from the experiments, 567 W. Besides, P is split between slot-windings and end-windings, with respect to their volume, which yields (15) and (16):

$$P_{slot} = \alpha P$$
$$P_{end} = \frac{1}{2}(1-\alpha)P \tag{15}$$

$$\alpha = \frac{\mathcal{V}_{slot}}{\mathcal{V}_{slot}+2\mathcal{V}_{end}} \tag{16}$$

Where $\mathcal{V}_{slot}$ is the total volume of slot-windings, $\mathcal{V}_{end}$ is the volume of each end-winding (the rear and front end-windings of the motor are considered to have the same volume), P_{slot} is the fraction of P generated inside $\mathcal{V}_{slot}$, P_{end} is the fraction of P generated inside $\mathcal{V}_{end}$, and α is the volume ratio between slot-windings and end-windings.

Once we know the values for P and α, P_{slot} and P_{end} can be derived from equation (15) and (16), and be integrated in the LPTN model. Motor-CAD® does this calculation for us. Here, $\alpha = 62\%$ and $P = 567\,W$. P_{slot} and P_{end} can now be calculated which yields: $P_{slot} = 351.5\,W$ and $P_{end} = 107.7\,W$.

3.1.2.2 Stator lamination thermal conductivity

The stator stack is made of silicon steel sheets (also called electrical steel) separated by a thin layer of coating material called the inter-lamination layer. In fact, this coating layer is not an independent material but is created when the silicon steel sheet are treated. Consequently, the equivalent thermal conductivity k_{int} of this inert-lamination layer is

hard to predict [50]. To overcome this issue, k_{int} was defined as a function of stator stack equivalent thermal conductivities (see values Table 2), and silicon steel thermal conductivity k_{steel}. These thermal conductivities are much easier to measure than k_{int}. In the following paragraph, we show how the relations between the different thermal conductivities were derived.

The successive silicon steel and inter-lamination layers of the stator stack can be seen in Figure 11. The laminations are positioned in (X, Y) plane normal to the axial direction of the motor (Z-axis in Figure 11). The individual thermal resistance of each layer is a function of thickness, area of the surface normal to the heat flow direction and the thermal conductivity of the material. As we are considering the heat flow along each axis, we will have different resistance values of the same layer for a different axis. Indeed, the area and thickness along two different axes can change. Based on the notations used in Figure 11, thermal resistances are defined as:

$$X \to R_{steel_X} = \frac{l}{k_{steel} A_{steel_X}}, R_{int_X} = \frac{l}{k_{int} A_{int_X}} \tag{17}$$

$$Z \to R_{steel_Z} = \frac{e_{steel}}{k_{steel} A_Z}, R_{int_Z} = \frac{e_{int}}{k_{int} A_Z} \tag{18}$$

Where R_{steel_X}, R_{steel_Z}, A_{steel_X}, A_Z are the steel sheet resistances and cross-sectional areas normal to the X and Z axes, respectively, and R_{int_X}, R_{int_Z}, A_{int_X} are interlamination resistances and cross-sectional areas normal to the X and Z axes, respectively. One can note that the Y direction is not considered here as the resistance definition the same as for the X direction due to inherent symmetry.

Two other useful dimensions must be defined:

$$A_X = nA_{steel_X} + (n-1)A_{int_X} \tag{19}$$

$$L = ne_{steel} + (n-1)e_{int} \tag{20}$$

Where A_X is the total cross-sectional area of the stator stack normal to X axis, L is the total length of the stator stack along Z axis and n is the total number of steel sheets.

Along the X direction, thermal resistances between each layer are in parallel whereas along the Z direction, thermal resistances are in series, as drawn in Figure 11. This observation yields equations (21) and (22) which define the stator stack equivalent thermal resistances R_X and R_Z respectively.

$$\frac{1}{R_X} = \frac{n}{R_{steel_X}} + \frac{n-1}{R_{int_X}} \tag{21}$$

$$R_Z = nR_{steel_Z} + (n-1)R_{int_Z} \tag{22}$$
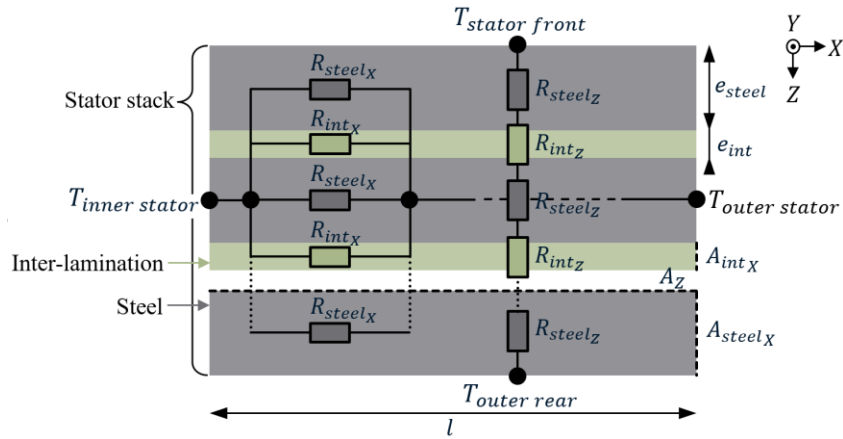
Figure 11 – Stator laminations cross-section view where Z-axis is along the axial direction of the stator.

Stator stack equivalent thermal conductivities k_X (along X axis) and k_Z (along Z axis) can be expressed as a function of R_X and R_Z respectively:

$$k_X = \frac{l}{R_X A_X} \qquad (23)$$

$$\frac{1}{k_Z} = \frac{R_Z A_Z}{L} \qquad (24)$$

The stacking factor S_f is defined as the ratio of cross-sectional area of silicon steel to the overall cross-sectional area of stator laminations. We can use our notations from Figure 11 to come up with the expression of S_f as follows:

$$S_f = \frac{n A_{steel X}}{A_X} = \frac{n e_{steel}}{L} \qquad (25)$$

For the Nissan Leaf electric motor stator, $S_f = 0.97$ [53]. Combining equations (17), (19), (21), (23), (25) yields equation (26) and combining (18), (20), (22), (24), (25) yields (27) given below. Again, inherent symmetries imply $k_X = k_Y$.

$$k_X = k_Y = S_f \times k_{steel} + \left(1 - S_f\right) \times k_{int} \qquad (26)$$

$$\frac{1}{k_Z} = \frac{S_f}{k_{steel}} + \frac{1 - S_f}{k_{int}} \qquad (27)$$

In Motor-CAD®, k_{steel} and k_{int} are used as input values. k_{steel} and k_{int} are derived from (26) and (27) with respect to k_X, k_Y and k_Z values. In order to have a fair comparison with the FEA model, k_X, k_Y and k_Z values are taken from Table 2. Solving (26) and (27) for k_{int} and k_{steel}, we have the thermal conductivity input values for our LPTN:

$$\begin{cases} k_{int} = 0.054 \ W.m^{-1}.{}^{\circ}C^{-1} \\ k_{steel} = 23 \ W.m^{-1}.{}^{\circ}C^{-1} \end{cases}$$

3.1.2.3 Slot-windings equivalent thermal conductivity

The copper wires used for the windings have a diameter $D_c = 0.800 \ mm$ and a total diameter (including insulation) $D = 0.885 \ mm$. Maximizing the number of wires which can fit inside a single slot of the Leaf motor leads to a maximum copper slot fill of 52%.

In the LPTN, the slot-windings are represented as a set of cuboids. The cuboid material includes the copper from the wire, the wire insulation, and the impregnation material. One cuboid contour is highlighted in Figure 12(b). One can notice that each cuboid can have a different height or width. However, they all have the same axial length equal to the length of the active windings which is also the length of the stator. Using cuboids instead of individual wires allows to have a much faster model. Moreover, this cuboid model is not affected by the randomness of the wire distribution in the slot.

The cuboid nodes are represented in Figure 12(a). This cuboid internal resistance network is defined as the rectangular prism model presented in Figure 3 from CHAPTER 2. In our LPTN, the windings are modelled as a set of 10 cuboids to account for the temperature gradient inside the slot. This set of 10 cuboids is represented by a single yellow resistor labelled *Slot winding* in Figure 10.

The internal resistance values between the face nodes and the center node are calculated from the equivalent thermal conductivities of the wire and impregnation material

along each axis. In order to have a good comparison of LPTN results with the FEA results, we used user-defined equivalent thermal conductivities which values are given in Table 2.
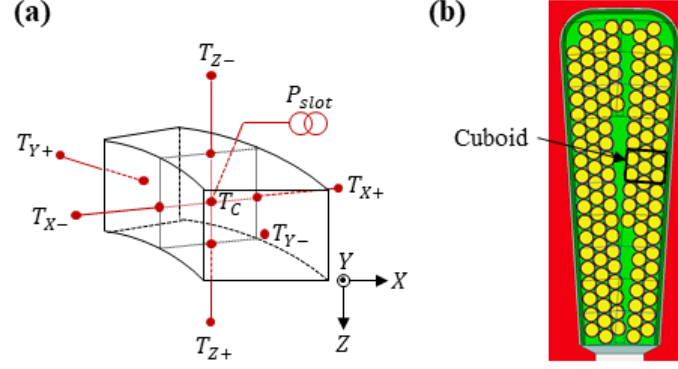
Figure 12 – Slot-windings cuboids: (a) 3D model representation, (b) in-plane representation within Motor-CAD® environment.

3.1.2.4 End-windings equivalent thermal conductivity

End-windings are modeled as a single toroid. The thermal resistance at the interface between each end-turns and the end-winding shape irregularities are therefore not considered. End-windings are modelled by 10 cuboids connected to the slot-winding cuboids on $T_{Z\pm}$ nodes. As a significant portion of a single wire in the end-winding is oriented along the tangential direction, the thermal conductivity along this tangential direction is significantly increased compared to the slot-winding thermal conductivity along the same direction. However, the thermal conductivity along the axial direction is decreased. This observation explains the different thermal conductivity values given in Table 2. As FEA and LPTN models must be accurately compared, user-defined values of end-winding thermal conductivities (taken from Table 2) were used inside Motor-CAD®.

3.1.2.5 Stator-to-housing thermal conductance

Thermal contact resistances are the most critical parameters in the LPTN model, as they are the main source of error due to manufacturing process uncertainties [3]. For example, the stator external surface roughness has a significant impact on the effective thermal contact conductance between the lamination stack and the housing [51]. Usually, a stator-to-housing air gap is used to account for the surface roughness. An air gap value for a good contact at the lamination-housing interface is around $0.01\ mm$ [13]. If we convert this air gap into an equivalent thermal contact conductance, we obtain a stator-to-housing conductance of $3,171\ W.m^{-2}.°C^{-1}$ for the Leaf motor.

In our case the thermal conductance is $5,555\ W.m^{-2}.°C^{-1}$ from Table 2. This thermal conductance corresponds to a mean gap of $0.006\ mm$. This suggests that the stator-to-housing contact conductance of the Nissan Leaf motor is better than usual good contact values from [13]. Nevertheless, this suggestion must be used carefully, as the value from the FEA model in Table 2 was derived from a temperature measurement based on a sample of the stator laminations, and not directly on the motor [51]. As this value was still consistent and as we wanted the same values between the FEA and LTPN, we kept the conductance value from Table 2.

3.1.2.6   Slot-liner contact

Slot-liner contact resistance is the contact between winding (in fact, the impregnation material overlaying the winding) and stator laminations. The thermal resistance is due to several manufacturing and assembly processes which yield imperfections, along with high uncertainties in the measured value of this resistance [54].

The accurate prediction of the thermal contact resistance has been proven to be highly critical in the prediction of the machine thermal behavior [13, 54].

In the real motor-assembly, we have a contact conductance for the winding side of the liner $G_{Liner-Wdg}$ and a contact conductance for the lamination side of the liner $G_{Liner-Lam}$. An equivalent thermal contact conductance of the liner G_{Liner} can be defined from $G_{Liner-Wdg}$ and $G_{Liner-Lam}$:

$$G_{Liner} = \left(\frac{1}{G_{Liner-Lam}} + \frac{1}{G_{Liner-Wdg}}\right)^{-1} \tag{28}$$

In Motor-CAD®, in order to represent the equivalent thermal contact resistance of the liner, an additional thin impregnation layer is considered between the liner and the laminations. The impregnation thermal conductivity combined with a goodness factor can represent the thermal conductance defined in (28). Consequently, in the LPTN, the thermal resistance associated with G_{Liner} is defined as the equivalent resistance of a 0.1 mm layer of impregnation between the liner and the stator lamination multiplied by a goodness factor of 0.051. The very low value of this goodness factor shows that considering a perfect contact with the liner is questionable if an accurate LPTN is needed.

They may be several explanations for the low thermal contact conductance at the liner interface. First, the roughness of the lamination stack surface and liner surface could increase the mean gap between these surfaces and, therefore, increase the resistance. Second, due to a relatively high viscosity of the varnish during winding impregnation process, they may be stuck air bubbles between the winding and the liner, further

deteriorating the contact goodness. Third, there is no additional pressure on the liner that would improve the effective contact area with the laminations or the windings.

In Figure 10, two resistors are associated with the liner-to-lamination contact resistance: one is for the contact with tooth slot side and the other is for the contact with slot bottom.

3.2   Results and discussion

Temperature results from experiments, FEA model and LPTN model are compared and discussed first. In the second part, a sensitivity analysis of each main thermal resistance from the LPTN is presented and discussed.

3.2.1   LPTN model and experimental data

After performing the LPTN simulations, we compared in Figure 13 the temperatures from experiments and the LPTN at the same locations. Labels used for each bar in Figure 13 come from Figure 6. The same reference temperature of 65 °C (coolant mean temperature) is used for both LPTN and experiments. As a reminder from Figure 6, one temperature corresponds to the average at different points, from symmetry considerations. Thus, one can derive the standard deviation for each of the five labeled temperatures in Figure 13. These standard deviations are represented by error bars in Figure 13. Standard deviations for each temperature associated with the end-windings are larger than for the *Housing* or the *Stator inner face*. Whereas the housing or the stator can be considered as orthotropic materials, end-windings are made of several bent wires with various trajectories assembled with impregnation which can contain air bubbles. Moreover,

there are non-equal spaces between end-turns. Therefore, end-windings are highly anisotropic and the assumed symmetry along the tangential direction of the end-windings implies these larger standard deviations.

In order to compare LPTN and experimental results, we can compute the relative error between LPTN and experimental results for each temperature. End-windings suffer from the highest relative error. Indeed, characterizing end-windings as a single toroid involves significant simplifications as, in the real end-windings, there are three layers of end-turns along the radial axis accounting for the three phases. In these end-turns, wires are curved to go from one slot to another and create a loop which makes the thermal conductivity of end-windings highly position-dependent. As a result, considering a fixed thermal conductivity along each axis of a cylindrical coordinate system in a single toroid is a strong simplification compared to real end-windings. Consequently, this yields the temperature differences between the LPTN and the experiments. Despite all these simplifications, we obtain a maximum relative error of 3.6% which demonstrates a good agreement between experimental data and LPTN results. Accordingly, we can claim that the LPTN model is able to accurately predict the steady-state temperatures of the Nissan Leaf motor.
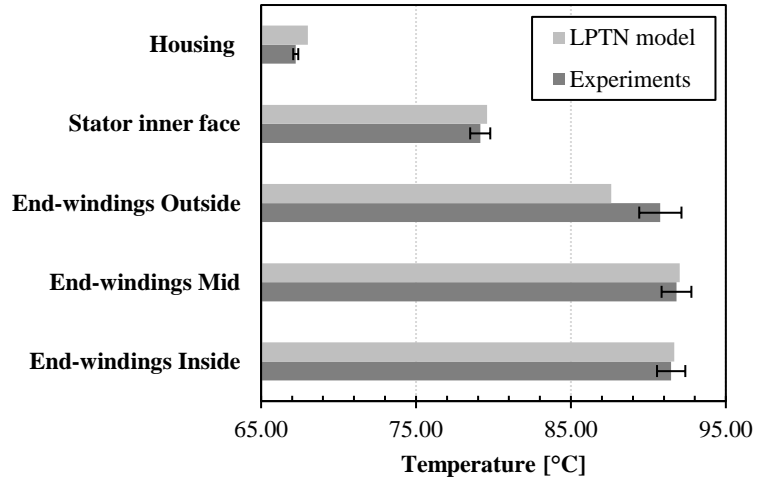
Figure 13 – Measured temperatures compared to LPTN output temperatures at 5 different points of the stator. Coolant mean temperature of 65 °C is used for both LPTN and experiments.

3.2.2   LPTN model and FEA model

The results from the FEA steady-state thermal analysis are shown in Figure 14. The comparison between LPTN and FEA models relies on temperature profiles along three different paths represented in Figure 15. Path (1) crosses the slot-windings and stops at the cooling channel wall, path (2) crosses the tooth and stops at the cooling channel wall and path (3) crosses the mid plane of the end-windings along the radial direction.

In order to have a better visualization for the comparison, temperature profiles from FEA and LPTN are given in Figure 16 for path (1), Figure 17 for path (2) and Figure 18 for path (3). For each of these figures, temperatures from experiments (see Figure 13) have also been reported. As presented in the previous section, LPTN representation of windings is based on cuboid structure. For Figure 16 and Figure 18, the cuboid temperature node which was used for the plots is T_c (see Figure 12), namely the temperature of the cuboid's

center node. In order to have an idea of temperature extremum for each cuboid, the maximum and minimum temperature envelope has been plotted as grey dotted lines on both Figure 16 and Figure 18. These envelopes are associated with the cuboid model in the LPTN which is only used for windings, thus, the dotted line is plotted only for the slot-windings part on Figure 16. Looking at the domain between these two envelopes is more relevant when comparing the LPTN model to experimental data or FEA model since the plot of T_C temperature does not correspond necessarily to the exact same temperature point in the FEA model or in the experiments.
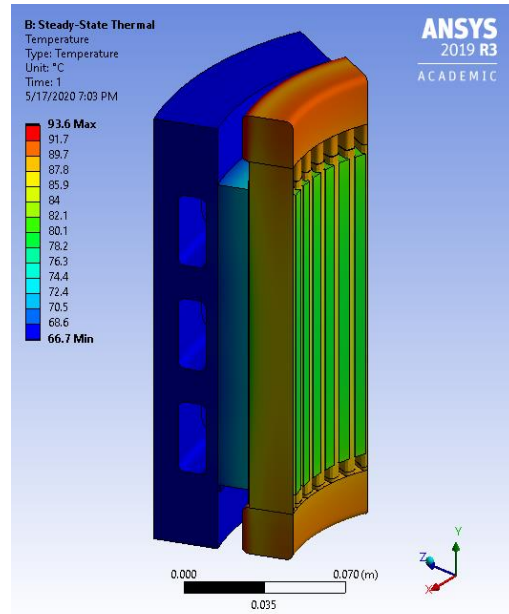
Figure 14 – Stator temperatures from FEA steady-state thermal simulation.
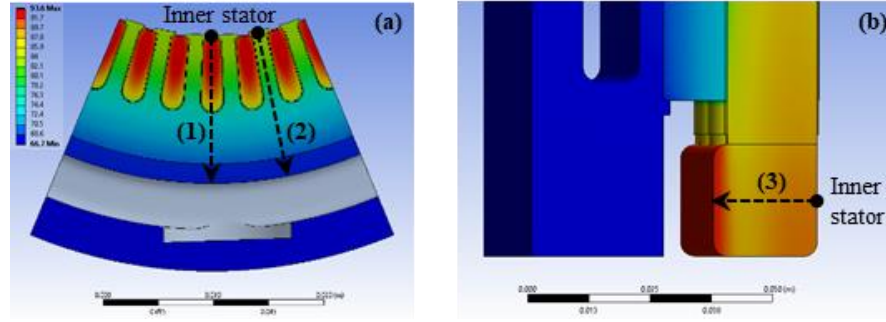
Figure 15 – Temperature profile paths: (a) path (1) and path (2) locations in the midplane cross-section view of the stator and (b) path (3) location in the axial cross-section view of the stator.

The maximum relative error between LPTN and FEA models for each path is given in Table 3. The overall maximum relative error is about 2% which makes the LPTN highly consistent with the FEA results for the regions where we have critical temperatures in a motor, namely slot-windings, stator tooth and end-windings. This confirms the ability of the LPTN to replace an FEA model for steady-state thermal analysis of an electric machine. The computational time for the LPTN steady-state analysis is about 4 seconds, whereas the FEA computational time, with the same computer configuration, is about 52 seconds. However, the LPTN inherent structure provides far coarser temperature resolution than the FEA model.

Thermal design of an electric motor is mainly focused on the highest temperature in each of its parts. Indeed, especially for the stator, the thermal limit is fixed by the temperature limit of the windings due to the wire insulation deterioration. As a result, having a number of temperature points is not essential as long as the maximum temperature values in each part are accurately predicted. The accuracy has been shown to be significantly high especially along path (2). For this path, we are only crossing stator

laminations and the housing. Stator laminations can be accurately model within a LPTN as they are composed of steady distributed silicon iron sheets.

Table 3 – Maximum relative error between FEA and LPTN model temperature profiles.

Path	Error
$(1) \rightarrow$ slot-windings	0.95 %
$(2) \rightarrow$ stator tooth	0.52 %
$(3) \rightarrow$ end-windings	2.08 %

The highest error occurs in the end-windings (Figure 18). We have already discussed the difference between end-windings LPTN model with a single toroid and fixed orthotropic thermal conductivity and the real end-windings in the *LPTN model and experimental data* section. The FEA model also uses a single toroid and fixed orthotropic thermal conductivity; however, the LPTN and FEA temperature profiles are reversed in the region beyond 17 mm from the inner stator.

The reason for this temperature rise in the FEA model comes from the low radial thermal conductivity value compared to the axial, and tangential thermal conductivities in the end-windings, see Table 2. For a more detailed explanation, end-windings volume can be represented as a combination of two volumes $\mathcal{V}_1$ and $\mathcal{V}_2$ as shown in Figure 19. Here $\mathcal{V}_2$ is the volume beyond 17 mm. As can be noticed in Figure 19, the heat flux q_2 from $\mathcal{V}_2$ to $\mathcal{V}_1$ occurs along the radial direction and unlike $\mathcal{V}_1$, $\mathcal{V}_2$ is not directly connected to the slot-windings. As a result, the heat produced in $\mathcal{V}_2$ leaves through surface A_2 (convection is neglected). Yet, the thermal conductivity along the radial direction is much lower than that along the axial direction – the direction of heat flux q_1 from $\mathcal{V}_1$ to the slot-windings.

This results in a temperature increase in $\mathcal{V}_2$ away from A_2 in the radial direction. However, from Figure 18, the temperature is decreasing within $\mathcal{V}_2$ for the LPTN model. Indeed, as for the slot-windings, end-windings are represented as a set of cuboids within the LPTN model, each connected to the slot-windings cuboids on their $T_{z\pm}$ nodes (see Figure 12). It means all cuboids are directly connected to the slot-windings, and thus, there is no equivalent volume $\mathcal{V}_2$, as for the FEA, which is not directly connected to the end-windings. Within the LPTN, the end-windings are represented as a single volume $\mathcal{V}_1$. This explains why LPTN temperature profile is still decreasing as we go beyond the bottom of the slot-winding.

Eventually, in Figure 18, the LPTN predictions are closer to the experiments. This is consistent since all wires that are in volume $\mathcal{V}_2$ come from the slot-windings. Thus, in the real end-windings, heat flux follows the curved path of the wires which make volume $\mathcal{V}_2$ directly connected to the slot-windings, hence the lower temperatures experimentally observed outside of the windings.
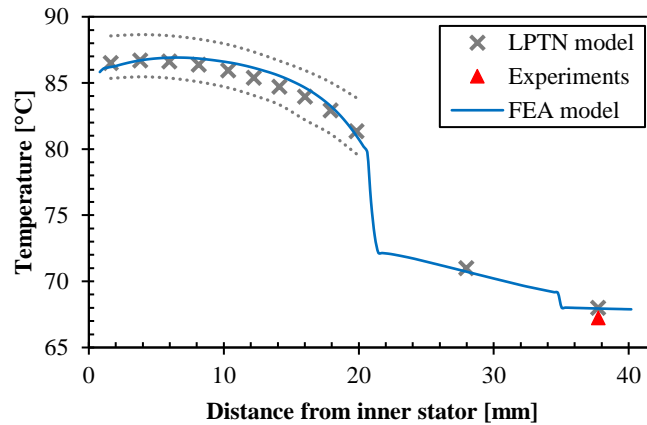
Figure 16 – Temperature profiles along a slot following path (1). Profiles are given for the FEA model, LPTN model and experimental data.
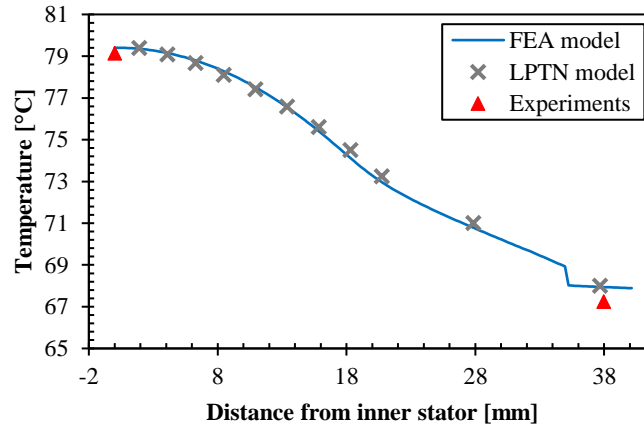
Figure 17 – Temperature profiles along a tooth following path (2). Profiles are given for the FEA model, LPTN model and experimental data.
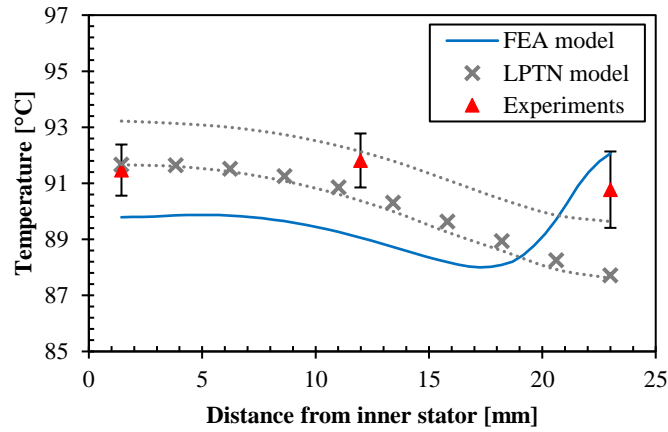
Figure 18 – Temperature profiles along end-windings following path (3). Profiles are given for the FEA model, LPTN model and experimental data.
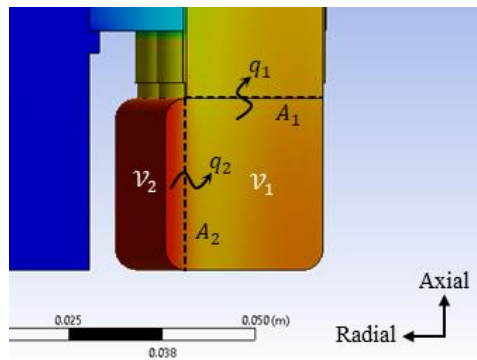
Figure 19 – End-windings heat flux and volume separation.

3.3   Sensitivity analysis

A sensitivity analysis using the LPTN can help identify the resistances most responsible for the temperature rise in the stator [47]. Usually, for a sensitivity analysis the thermophysical properties of the different materials are considered [55]. However, because both thermal conductances and thermal conductivities are considered here, the present sensitivity analysis is based on their equivalent thermal resistance. The final thermal parameters and their associated thermal resistance names chosen for the present sensitivity analysis are given in Table 4.

Table 4 – List of thermal resistances used for the sensitivity analysis, and their related initial thermal parameter.

Thermal resistance	Associated thermal parameter
R [Liner Contact]	Liner-to-lamination thermal contact conductance
R [Liner]	Liner thermal conductivity
R [Slot-Windings]	Slot-windings equivalent thermal conductivity
R [Water-Jacket]	Channels heat transfer coefficient
R [Housing Contact]	Housing-to-lamination thermal contact conductance
R [Housing]	Housing thermal conductivity

The LPTN used for the sensitivity analysis was based on a 20% and 50% value reduction for each thermal resistance in   Table 4. The sensitivity was assessed by computing the temperature difference ΔT between the winding maximum temperature with initial resistances and the winding maximum temperature with the new reduced resistance. Figure 20 presents the results of the sensitivity analysis for each resistance and each percentage reduction.

Figure 20 shows that the *Liner Contact* resistance has the highest influence on the temperature variation of the motor, followed by the *Liner* resistance. This high influence of the liner relates to the highest temperature decrease ($\approx 7°C$), at 21 mm from the inner stator in Figure 16. This temperature decrease occurs along a very short distance, less than 1 mm, corresponding to the liner area.

The liner influence is due to the low thermal conductivity of the liner compared to other thermal conductivities involved (see Table 2). Also, this influence comes from the low contact thermal conductance of the liner compared to other thermal conductances like the stator-to-housing contact conductance. Although the difference between contact thermal conductance of the liner compared to other conductances seems quite high, it remains consistent. Indeed, stator-to-housing thermal resistance is essentially caused by laminations roughness. At the lamination-to-liner interface, this same roughness is responsible for a decrease in the contact conductance. However, imperfections during impregnation process, as well as remaining air between the liner and the laminations significantly impact further reduction of the liner contact conductance.
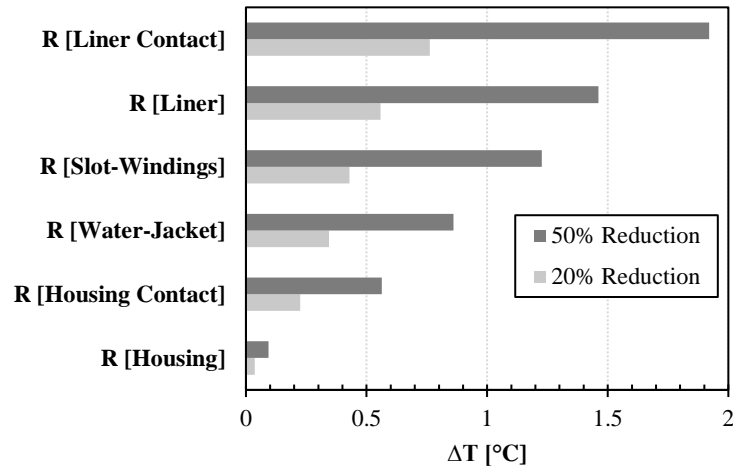
Figure 20 – Sensitivity analysis of the LPTN thermal resistances for 20 % and 50 % value reductions.

It is worth noticing that *Water-Jacket* resistance sensitivity is less than half of the *Liner Contact* resistance sensitivity. This shows that improving the heat transfer coefficient of a cooling jacket system outside of the slot-windings has some limitations in terms of maximum temperature reduction. This is particularly illustrated in Figure 21. The limitation of increasing the heat transfer coefficient is represented by the dashed line asymptote equal to 91.50 °C. Therefore, the maximum temperature difference between the current heat transfer coefficient ($1,428\ W.m^{-2}.{}^{\circ}C^{-1}$) and an infinite heat transfer coefficient is about 1.7 °C.
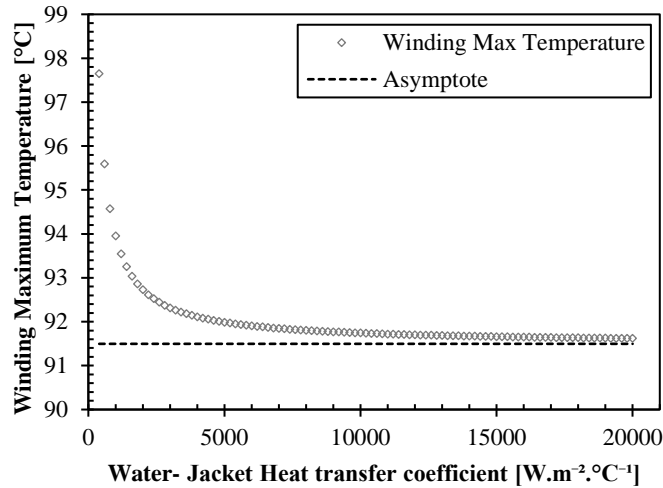
Figure 21 – Winding maximum temperature as a function of water-jacket heat transfer coefficient. Results are computed with our LPTN model.

From the previous observations, we can draw an important conclusion. The next-generation cooling systems that will make IPM motors reach high power densities must be between the liner and the windings. According to the sensitivity analysis, improving the water-jacket heat transfer coefficient or the stator-to-housing conductance will not provide enough temperature decrease in the windings. With this analysis, one can understand that the next generation of high-density electric motors must have these direct winding cooling as presented in the Introduction of this thesis. Hence, the development of the end-winding cooling system presented in the following chapter.

CHAPTER 4.   DESIGN, TESTING AND MODELLING OF THE END-WINDING CHANNEL

In the previous chapter, the sensitivity analysis has shown that reaching the next level of high-power density in electric machine would require to have a direct cooling method of the windings. As the end-windings represent the hot-spot of the windings as shown in Figure 18, we have decided to focus on creating a new cooling system for the end-windings. Different types of end-winding cooling systems have been described in the Introduction of this thesis. Each of them has its own drawback. The oil spray cooling has a high overall heat transfer coefficient, but it requires a second flow loop in addition to the WEG loop and can accumulate some dust over a long period of time. The potting material does not need a second loop and has a good overall heat transfer coefficient. However, a lot of potting material is needed to pot all the end-winding region which can lead to higher costs. Moreover, for high volume production the potting process can be hard to manage. The trade-off between all these end-winding cooling solutions would be to have a cooling system which does not need an additional flow loop, can use the same coolant used for the water-jacket, can be easily mass produced, and does not represent a high cost compared to that of the motor. In [19], Vincenzo Madonna proposed a promising solution of using a tube inserted inside the end-windings. However, this solution presents some important drawbacks developed in the Introduction of this thesis. We have decided to adapt the solution to create an improved cooling system based on a U-shaped end-winding channel with rigid material to match the scalability and distributed end-winding compatibility requirements.

4.1 End-winding channel design and fabrication

4.1.1 Design requirements

The end-winding channel design was based on the geometry of the Nissan Leaf motor. This motor has distributed windings as most of the motors inside electric vehicles. Consequently, the toroid formed by the end-turns is quite compact which makes it difficult to push a channel inside the windings. Moreover, during electric machine manufacturing, once wound, the windings are impregnated with a varnish material which is then cured, creating a solid toroid which cannot be deformed to insert channels as it was done in [19]. Thus, putting channels inside the windings would require changing the impregnation process of the winding. If we want our solution to be suitable for mass production, we need to have cooling system that can be assembled in the motor after the impregnation process.

The coolant flowing through the channel must be the WEG mixture as we want to keep the same coolant used for the water-jacket. This WEG is electrically conductive. Consequently, we must have a perfectly sealed channel to prevent any WEG leak on the windings. Furthermore, the thermal resistance between the coolant and the end-windings needs to be as low as possible to ensure a good heat transfer. This implies that the channel walls should be as thin as possible and as close as possible to the windings. However, we must ensure a minimum wall thickness for the channel to withstand the internal pressure from the coolant at high flow rates. The pressure requirement was fixed at 15 psi based on the cooling loop total pressure.

The wall of the channel cannot be made of conductive material as we are touching the end-windings and we may have risks of short circuits. Moreover, this non-conductive

47

material must withstand high temperatures. The maximum operating temperature for the material should be equal to the maximum temperature rating from the wire insulation class given by the NEMA standard. We have considered a class F rating for the windings leading to a maximum operating temperature of 155°C. Eventually, the contact area between the channel and the end-winding needs to be as high as possible to enhance the heat transfer from the windings to the coolant.

4.1.2   Design choices

In addition to the requirements listed in the previous section 4.1.1, the design of the end-winding channel has been limited by cost, time, and equipment constraints. We had only 3 months to create and test the end-winding channel prototype at NREL. Due to this time and costs constraints, and as we needed several iterations on the channel dimensions before being able to test the final prototype, we could not outsource the fabrication of the end-winding channel. Consequently, we had to use the available equipment from NREL to manufacture the end-winding channel prototype.

In order to maximize the surface contact area between the channel and the end-windings, we decided to design the channel as a U-shape surrounding the end-windings. With this U-shape we are in contact with the inner side, outer side and top side of the end-windings while having an easy insertion process.

The material for the channel needed to be non-conductive with a high temperature operating point of 155°C. PEEK material and ULTEM are two polymers which have a wide operating temperature range. In our case, both PEEK and ULTEM have maximum operating temperatures higher than the maximum operating temperature of the winding

(155°C). In terms of equipment, the easiest way to create a prototype and iterate quickly on different sizes and shapes is to use a 3D printing process. However, NREL had only a 3D printer capable of printing ULTEM 9085 parts. As a result, we decided to go with ULTEM 9085 material for the fabrication of the end-winding channel. ULTEM 9085 has a heat deflection at 264 psi of 153°C and a glass transition temperature of 186°C according to Stratasys manufacturer. As ULTEM is a high-operating-temperature material, Fused Deposition Modeling (FDM) is the preferred 3D printing technology for this material. FDM consists of a thermoplastic filament connected to a heated extruder head which moves along each cartesian axis of a 3D space. The part is extruded layer by layer. The thickness of one layer is limited by the diameter of the filament and the deposition speed.

3D printing is a fast iteration process, but it comes with some disadvantages in terms of design possibilities. Indeed, our first idea was to 3D print the channel as a single body as seen in Figure 22. However, 3D printing this geometry would have required a support structure inside the channel cavity to support the top wall of the channel perpendicular to the 3D printing direction. This support structure inside the channel would have increased the pressure drop significantly as well as the risk of low-quality sealing of the channel wall. Consequently, we decided to split this single body into two parts.
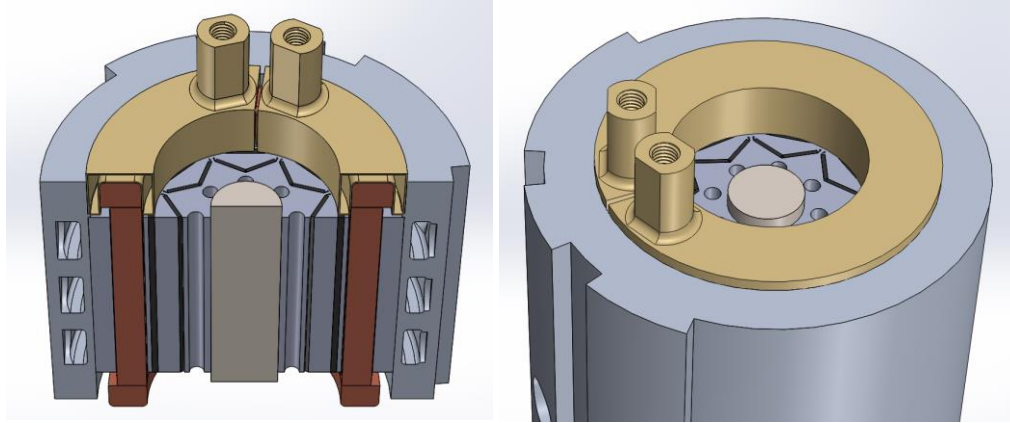
Figure 22 – Initial design of the end-winding channel.

The two resulting parts are shown in Figure 23 and Figure 24. The bottom part is inserted inside the end-windings. This part includes the U-shape cavity for the fluid to flow all around the end-windings. The top part is then fixed to the housing and pushed against the bottom part to ensure that the complete assembly is sealed. The inlet and outlet of the end-winding channel are located on the top part as shown in Figure 23. This was the easiest way to connect the end-winding channel to the rest of the coolant loop. However, in a fully integrated solution, these inlet and outlet could come directly from the housing and enter the channel from the outer side of the U-shape wall. On the left picture of Figure 24, one can see that the cavity has a separation wall which prevent the fluid from the inlet to be mixed with the fluid from the outlet.
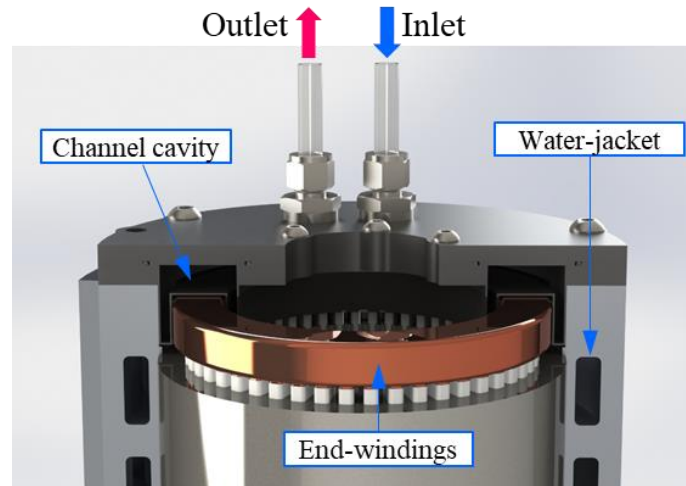
Figure 23 – Cross-sectional view of the final assembly of the end-winding channel and the Nissan Leaf motor
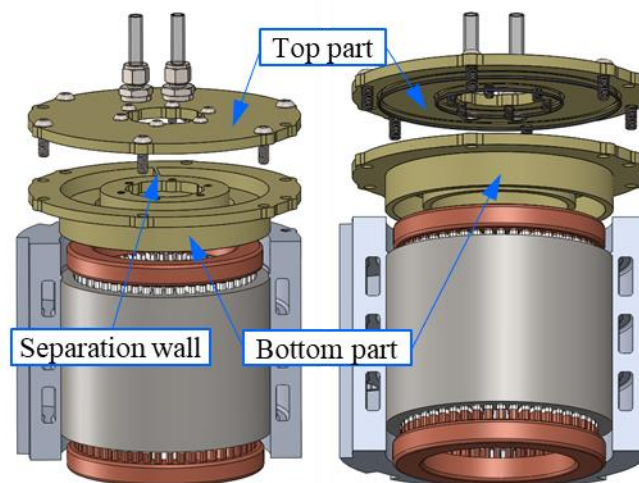
Figure 24 – Final design of the end-winding channel. The bottom part with the U-shape cavity is pushed to the end-windings and the top part is fixed to the bottom part and the housing.

The final dimensions of the end-winding channel are given shown in mm in Figure 25. As we can see the left and right sides of the U-shape channel have an internal thickness of 4.7 mm. We were limited by the distance between the housing and the channel. In a fully integrated design, we would increase the gap between the housing and the end-winding

channels to increase the thickness of the channel sides to further reduce the pressure drop across the end-winding channel.
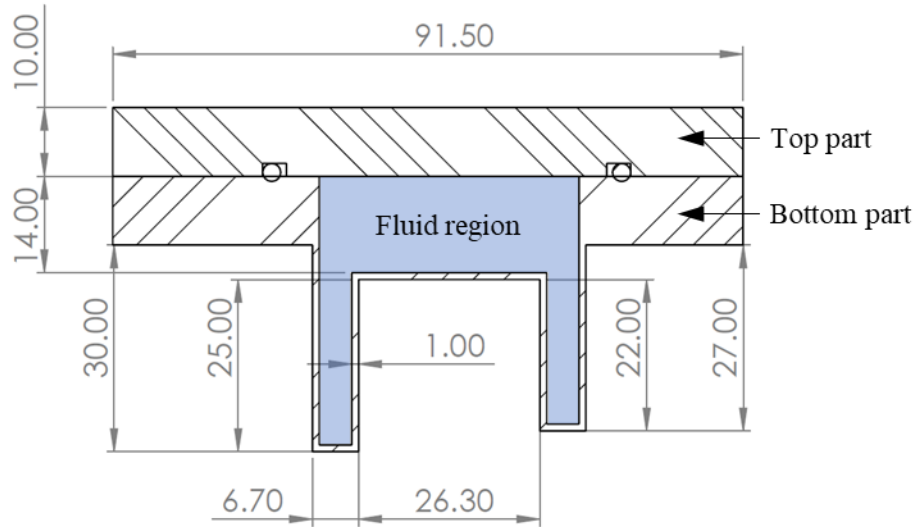
Figure 25 – End-winding channel cross-sectional view with dimensions in mm.

4.1.3   End-winding channel sealing

The end-winding channel must be perfectly sealed to prevent any WEG coolant from touching the end-windings. Our solution presents two different sealing challenges. The first challenge is the sealing of the parts them-selves. Indeed, the optimization of the filament deposition in the FDM process is not enough to ensure the watertightness of the 3D-printed parts. Tiny air gaps still exist between the deposited filaments especially at the corners and when two contours with different curvatures are next to each other. The second challenge is the sealing of the bottom and top part assembly. We must ensure that we have a perfect sealing when pushing the top part against the bottom part. Our solutions for these two challenges are presented hereafter.

4.1.3.1 Individual part sealing

In order to seal a 3D-printed part, the small air gaps between the filament needs to be filled so that the part become a solid block. Stratasys, the manufacturer of the 3D printer used for our parts, has released a Technical Application Guide [56] where various sealing methods for 3D-printed parts using FDM process are presented. When selecting a solution for our application, we must ensure that the sealing solution matches our design requirements. As a reminder, the final sealed part must withstand an internal pressure of 15 psi with no leaks and a maximum temperature of 155℃. To meet the pressure requirement, Stratasys team recommends using a two-part epoxy to make the 3D printed part watertight. Two types of epoxy are proposed: Loctite E-20HP Hysol Epoxy from Henkel Adhesive Technologies and the TC-1614 Epoxy from BJB Enterprises. Only the TC-1614 meets the temperature requirement for our application. Indeed, according to the TC-1614 Datasheet, this epoxy withstands temperatures up to 177℃ which is beyond our maximum temperature of 155℃. Moreover, the TC-1614 epoxy has been especially developed for 3D printed part sealing which was another reason to select this epoxy.

The TC-1614 is a low-viscosity two-part epoxy. A two-part epoxy is composed of a resin part and a hardener part. The resin and hardener are both liquid at ambient temperature. When this resin and hardener are mixed, they form a viscous epoxy which becomes solid after a few hours of curing. The principle of 3D printed part sealing with this type of epoxy is simple. After mixing the resin and the hardener, the still-liquid formed epoxy is applied to the 3D printed part. The epoxy penetrates the part and fills all the small airgaps. The epoxy cures inside the part and we eventually obtained a composite part made of epoxy and ULTEM with no airgap.

Nevertheless, the final complete process for 3D-printing part sealing with TC-1614 is more complex as it requires intermediate steps to ensure a good sealing quality and a good surface finish of the part. The complete process is shown in Figure 26. This process has been adapted from the initial process proposed by BJB Enterprises in their TC-1614 datasheet. One of the first important steps is step 2. Indeed, putting the hardener and resin separately in the oven, before mixing them, allows to reduce the viscosity of the resulting epoxy and help soak this epoxy in the part. The second important step is step 10 where the part is submerged in epoxy. It is essential to ensure that all the part surfaces are coated with epoxy to prevent any remaining air bubble inside the part after the sealing process. Steps 14 and 15 are the next essential steps of the process which allow to obtain a good surface finish of the part. Indeed, if some excess epoxy is left in corners or around the holes this will create excess thickness once the epoxy is cured. Having this excess thickness would mean that the dimensions and shape of the part are no longer the same, preventing our channel to be correctly assembled and pushed in the end-windings. Eventually putting the part in the oven at step 6 to cure the epoxy allows to obtain a final part with better strength which is suitable for our application considering channel internal pressure.

3D Printing Part Sealing Process

1. Set oven temperature at 45℃.
2. Put the 3D printed part in the oven for 15 min.
3. Set the oven temperature to 35℃.
4. Put the resin and hardener in separate containers.
5. Put the containers with the part in the oven for 15 min.
6. Remove the containers from the oven.
7. Set the oven temperature at 45℃.
8. Mix the resin and hardener in a single container.
9. Put the part in plastic bag.
10. Pour the epoxy in the plastic bag.
11. Zip the bag and make sure no air bubble is stuck between the epoxy and the part.
12. Put the bag with the part and the epoxy in the oven for 20 min.
13. Pull the part out of the bag and put the bag with remaining epoxy aside.
14. Drain off excess epoxy and brush the surface using foam brush to have a good surface finish.
15. Blow the surface with a hot air using a heat gun to remove tiny air bubbles stuck at the surface of the part.
16. Set the oven to 60℃.
17. Put the part in the oven and let the part cure for 6 hours.
18. Stop the oven and let the part cool down in the oven.

Figure 26 – Process used to seal the 3D printing parts with TC-1614 epoxy.

4.1.3.2   Assembly sealing

The first approach to seal the bottom and top part assembly was to use a static O-ring face sealing between these two parts. Two glands were designed on the outer side and inner side of the channel on the top part. These glands and the two O-rings used for the assembly can be seen on the right picture in Figure 24 or in the cross-sectional view in Figure 25. When using an O-ring solution, the surface finish of the gland surface should be

lower than 63 μm (RMS value) for the side surfaces of the gland and 32 μm (RMS value) for the bottom surface of the gland according to Parker O-ring Handbook [57]. However, these values are lower than the typical roughness obtained with a 3D-printing process. Indeed, according to the roughness study of 3D-printed parts using ULTEM 9085 from Fischer and Schöppner [58], the roughness for surfaces parallel to the extrusion direction (corresponding to a build angle of 90 degree as defined in their paper) is around 100 μm while the roughness for surfaces perpendicular to the extrusion direction (corresponding to a build angle of 0 degree as defined in their paper) is around 150 μm. Therefore, for both the sides and bottom of the gland, the surface roughness of 3D-printed parts using ULTEM 9085 are higher than the maximum surface finish recommended in [57].

To improve the surface finish of the parts, we decided to sand them using sanding sheets from medium to fine grit. This sanding step was performed once each part was filled with epoxy following the sealing process presented in section 4.1.3.1. Only the surfaces in contact with each other and the surfaces of the gland were sanded with care. For the other surfaces, surface finish did not have an impact on the sealing quality of the top and bottom part assembly. The result of the sanding surface finish can be seen in Figure 27 for the top and bottom parts. The matte surfaces correspond to the sanded surfaces while the glossy surface on the left picture is the original surface coated with epoxy. One can notice that the surface finish is really good on the visible sanded surface of the picture. While we have not measured the exact surface roughness, it obvious via touch, that we have a surface roughness lower than the maximum roughness recommended in the O-ring handbook [57].
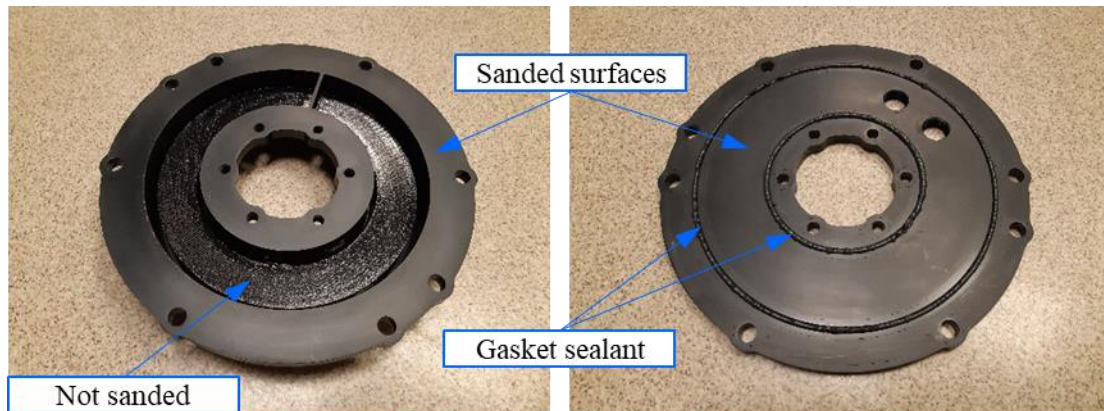
Figure 27 – Bottom (left) and top (right) parts of the end-winding channel after sealing with epoxy and sanding surface finish.

While the surface finish of the contact surfaces looks good enough to use an O-ring solution, we were not able to achieve the same finish quality for the gland. Indeed, using sanding sheet to smooth each surface of the gland was difficult and correctly sanding the corners of the gland was impossible. Consequently, we could still potentially have a leak at one of the O-ring after bolting the top part to the bottom part. To test the channel assembly sealed with O-rings before using it for the test, we used a Fluke 718 300G pressure calibrator. This pressure calibrator was connected to the outlet of the end-winding channel and the inlet was closed using an endcap fitting as shown in Figure 28. We just used this calibrator to have an accurate measurement of the pressure we were creating inside the channel by using the manual pump of the calibrator. Soapy water was applied on each external surface of the assembly to easily detect any leak.

Figure 28 – End-winding channel airtightness test setup

After increasing the pressure inside the channel using the manual pump, we detected a leak at 9 psi from the outer edge, at the interface between the bottom and top part. As a reminder from our design requirements, the channel must withstand a maximum pressure of 15 psi. Even though this test was measuring airtightness instead of watertightness, we could not take the risk to use an O-ring for the top and bottom part assembly knowing that we had an air leak at 9 psi. Increasing the number of bolts would have probably solve this sealing issue but we were constrained by the number of available holes in the Nissan Leaf housing. Thus, to solve this issue, we decided to replace the O-ring by a silicone gasket sealant commonly used in the automotive industry, namely the LOCTITE 5900 from Henkel Adhesive Technologies. We applied this silicone sealant in the glands of the top part as it can be seen in Figure 27. Then, we bolted the top part to the bottom part and let the sealant cure at ambient temperature for one day. We performed the same airtightness test shown Figure 28 for the new assembly with the gasket sealant, and we did not detect any leak at 20 psi. This solution was validated, and the end-winding

channel was ready to be fixed to the Nissan Leaf Housing. Two photos of the final end-winding channel assembly are shown in Figure 29
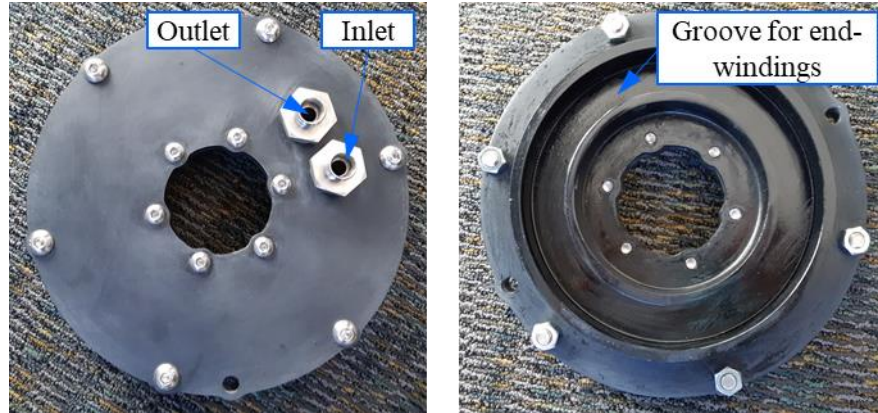
Figure 29 – Final end-winding channel assembly

4.1.4   Final assembly of the end-winding channel and the motor

The end-windings have a very irregular geometry due to the coil winding manufacturing process used for typical round wires. This can be observed in Figure 30. For instance, the gap between the outer side of the end-windings and the inner side of the housing is not constant. The difference between the minimum gap and the maximum gap is more than 1 mm which can have a significant impact on the heat transfer between the end-windings and the channel. This gap variation also exists on the inner side of the end-winding. Compressing the end-windings to form a better rectangular shape would help reducing the geometric irregularity. However, the motor we had was a purchased motor with windings already impregnated. Therefore, the end-windings were forming a very solid block which could not be reshaped.

Figure 30 – Nissan Leaf end-winding rear side view

For our cooling system to be used with this type of distributed windings, we then had to improve the contact between the channel wall and the end-windings to reduce the associated thermal resistance. For electronic cooling, a thermal paste is typically used between the hot electric component casing and the cold plate to have a better thermal contact. We decided to use this same technique by applying a thermal paste between the channel walls and the end-windings. After comparing different options, we end up using a thermally conductive cure-in-place silicone compound from Parker Chomerics called THERM-A-FORM™ CIP35. This silicone compound is particularly suitable for complex shape, it does not require high compressive force, can cure at ambient temperature and has a high thermal conductivity of 3.5 $W.m^{-1}.K^{-1}$. These are the main reasons for using this product.

As we did not know exactly what amount of silicone would be required to fill the irregular gap between the channel walls and the end-windings, we decided to spread the

silicone compound on the end-windings and then push the channel assembly on the end-windings. This would allow the excess potting to be pushed to the laminations of the stator. The potting was applied by hand and a spatula was used to smoothen the surface. Two photos of the end-winding with the silicone compound, just before inserting the channel, are shown in Figure 31. Alternatively, if the final amount of silicone required to fill the gap between the channel and the winding is known, it would be better to put the compound on the channel walls first and then push the channel assembly on the end-windings. In this case, we would use much less compound than what we have used for our experiments. It is difficult to have a good estimate of the effective compound volume in the end-winding region. We estimate we had ~250 cm^3 of silicone compound in the end-windings.
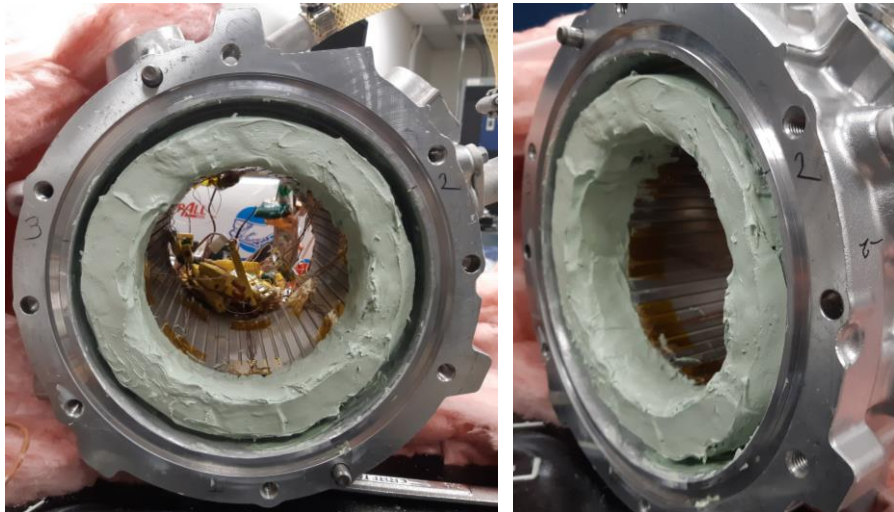
Figure 31 – Thermally conductive silicone compound on end-windings.

After applying the silicone to the end-windings, we pushed the end-winding channel assembly to the end-windings. We let the silicone compound cure in place for one day. The final assembly of the channel and the motor can be seen in Figure 32. The silicone layer in between the top of the end-windings and the channel prevented us from pushing the

channel up to the end-windings. As a result, we still had a gap of ~2 mm between the housing and the channel flange.
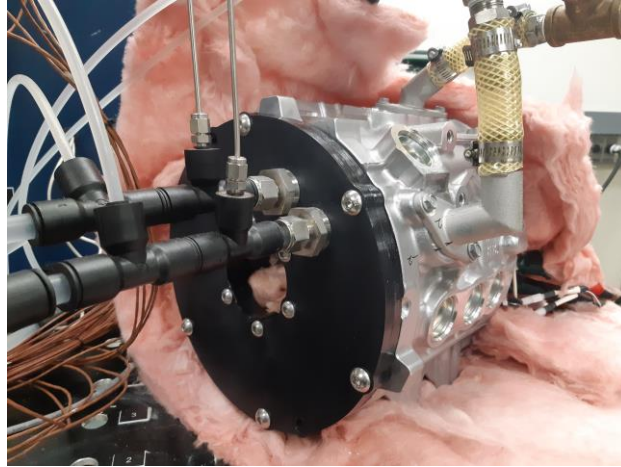
Figure 32 – Final assembly of the end-winding channel to the Nissan Leaf motor

4.2   Experimental setup and procedure

4.2.1   Cooling loop

Both the end-winding channel and water-jacket of the motor assembly were connected to the same cooling loop shown in Figure 33. The fluid used in this cooling loop was WEG mixture with 50% volume of water. The temperature of the fluid is stabilized at 65°C for the experiments by utilizing a chiller/heater circulator connected to the bath. The water-jacket and end-winding channel fluid paths are connected in parallel to control the flow through each path individually. The flow was controlled by changing the position of manual valves shown on the schematic (Figure 33). The total flow was set by changing the pump speed. The channel valve and the water-jacket valve are then used to control the flow

balance between the end-winding channel and the water-jacket. The total flow could be adjusted using the bypass valve as changing the pump speed does not provide an accurate control of the flow in the loop.
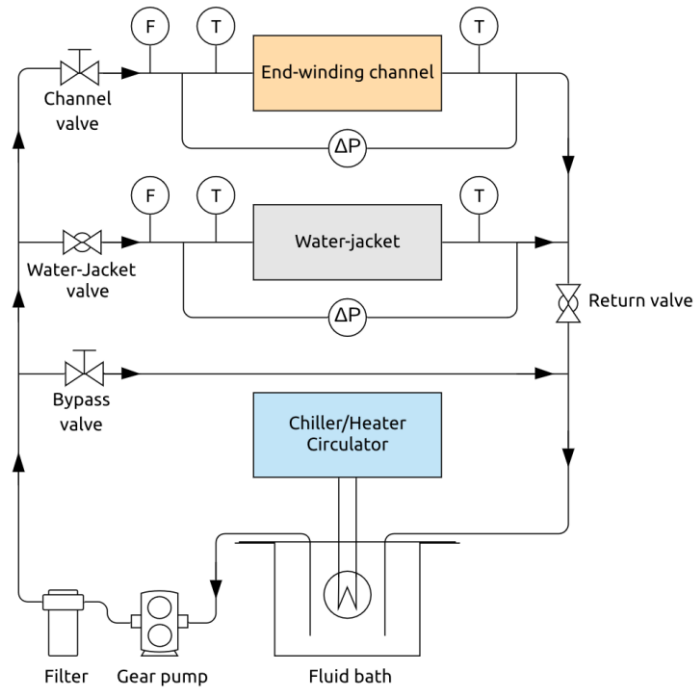
Figure 33 – Cooling loop schematic

In this cooling loop, we have two flow meters measuring the volumetric flow rate across the end-winding channel and the water-jacket. The pressure drop across each cooling system was also monitored via two pressure drop sensors. Also, the temperatures at the inlet and outlet of each cooling system were measured using K-type thermocouples.

4.2.2   *Motor temperature measurements*

The end-winding channel cooling system was located on the rear end-winding side. As a result, we wanted to maximize the number of thermocouples in this area to accurately measure the temperature distribution on the end-winding surfaces. To guide our choice of

the thermocouple locations, we decided to run DC current through each phase of the motor using one power supply per phase (same configuration as for the experiments). Each phase was supplied with the same current. No cooling loop was used. The objective of this quick test was to understand the temperature distribution in the end-windings using a FLIR thermal camera. Based on the information from the image that we got from the thermal camera (see Figure 34), we decided to divide the end-windings into 8 sections corresponding to the motor pole number. In each section the same temperatures were measured:

- Temperature at the rear end-winding outer surface normal to the radial direction of the motor (labelled "Rear End Outer").

- Temperature at the rear end-winding inner surface normal to the radial direction of the motor (labelled "Rear End Inner").

- Temperature at the rear end-winding top surface normal to the axial direction of the motor (labelled "Rear End Top").

- Temperature inside the gap between two end-turn in the middle of the end-winding (labelled "Rear End Inside").

The location of each thermocouple, following the temperature definitions given above, is shown in Figure 34. Each number represents one section. The inlet and outlet of the end-winding channel are represented by a red disc and blue disc, respectively. The picture in this figure is the distribution image captured with the thermal camera. Thus, a total of 32 temperatures are measured in the rear end-windings which allows us to capture the temperature range on each side of the end-windings. As these end-windings were

64

already impregnated, it was not possible to have a thermocouple inserted directly inside the end-windings to capture the maximal internal temperature. However, having end-windings impregnated using the real manufacturing process from the factory allows to have a good representation of the impregnation quality.
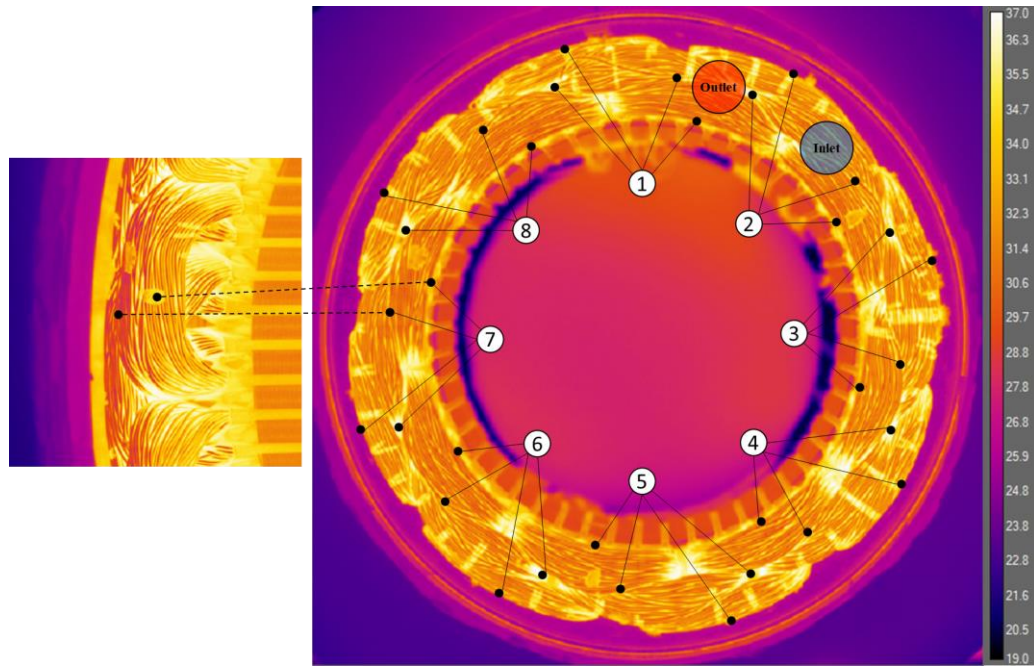
Figure 34 – Thermocouple location and temperature distribution in the rear end-windings. The end-windings are divided in 8 equal sections. The red disc and blue disc represent the outlet and inlet of the end-winding channel, respectively.

In addition to these 32 thermocouples, we placed 2 thermocouples on the front end-winding inner surface and top surface in sections 2 and 8, as well as a thermocouple at the ring terminal of termination wires.

The thermocouples used in the experiments are K-type thermocouples. All thermocouples were calibrated using a reference probe leading to a maximum uncertainty of $\pm$ 0.1°C for a temperature range from 20°C to 120°C. The uncertainty values for the

thermocouple calibration are given in APPENDIX A. The thermocouples were fixed on surfaces using a thermally conductive epoxy from Omega.

4.2.3 Complete experimental setup

The complete experimental setup for the motor cooling testing is shown in Figure 35. At the bottom of the photo, we can see the bath containing WEG coolant and the heater/cooler circulator which stabilizes the temperature of the bath. Just after the bath, we have the pump, at the bottom left corner. The rest of the cooling loop is behind the blue panel of the bench. On the right of this panel, we have the water-jacket valve which is connected to the water-jacket inlet. The gate valve with a red handwheel is the end-winding channel valve. The flow meter, pressure sensors and thermocouples are connected to a

National Instrument's CompactDAQ data acquisition system which can be seen at the right of the screen in Figure 35.
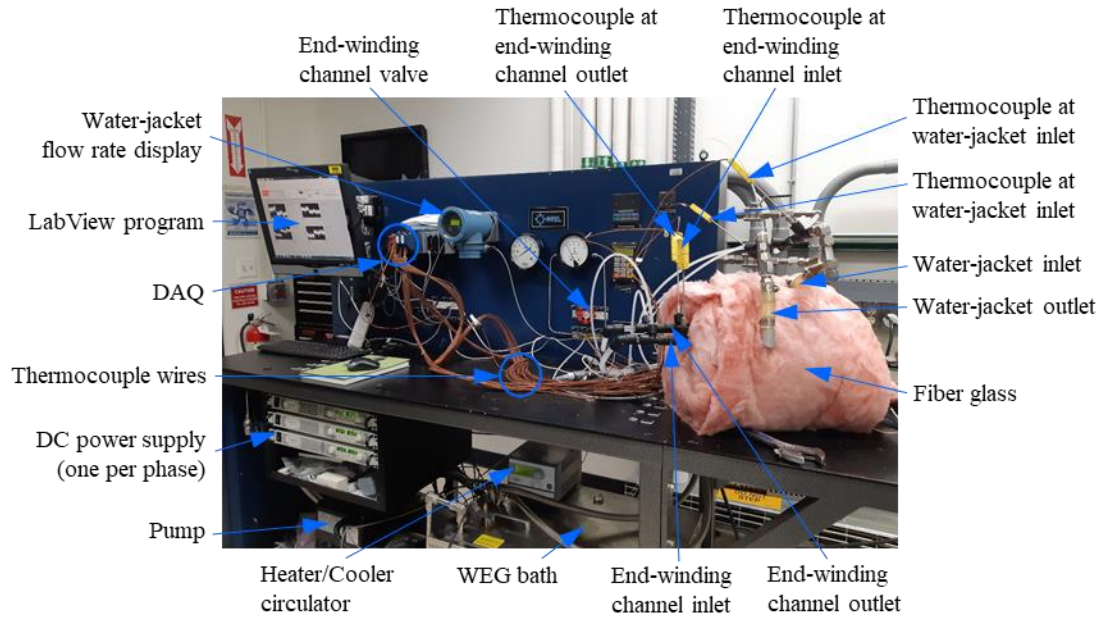
Figure 35 – Experimental apparatus for motor cooling testing using end-winding channel and water-jacket cooling systems.

The water-jacket, the front side and rear side of the motor were covered with fiberglass to minimize natural air convection on the external surface of the motor. The rotor was removed from our experiments and replaced by fiberglass. Due to this fiberglass, we could consider all external surfaces previously in contact with air as adiabatic. Each phase of the stator was supplied with a stabilized DC current of 160 A with a Y configuration (see schematic in Figure 36). We used one power supply per phase to ensure a good current balance between each phase. These power supplies were Agilent technologies N5762A (8V/165A, 1320W) and they can be seen just above the pump, on the left side of the photo in Figure 35.
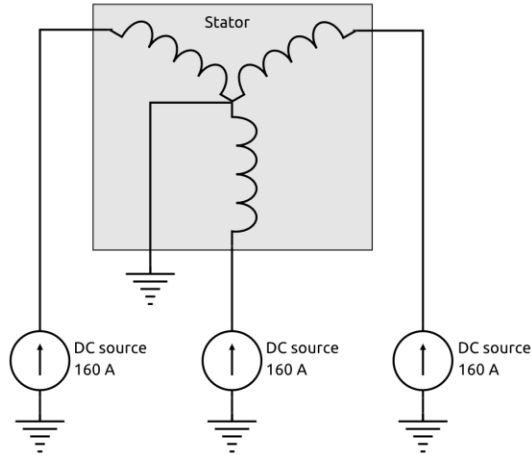
Figure 36 – Stator phase connection to DC power supply using Y configuration.

Finally, the experiments were monitored and controlled with a LabVIEW program connected to the DAQ system and the power supplies. Flow rates, pressure drops, thermocouple temperatures, phase current, phase voltage and electric power were monitored in this LabVIEW program.

4.2.4   Experimental procedure

The fixed parameters and variables in these experiments are given in Table 5.

Table 5 – Fixed parameters and variables for motor cooling experiments.

Fixed parameter	Value
Fluid temperature in the bath [°C]	65°C
DC current per phase [A]	160 A
Total input power [W]	530 W
Variable	**Values**
Water-jacket flow rate [L/min]	3, 6, 10
End-winding channel flow rate [L/min]	3, 6, 10

The only variable in these experiments were the flow rates in the end-winding channel and the water-jacket. To understand the impact of using the end-winding channel cooling system, on the stator temperatures, we needed a first set of tests without the end-winding channel, using the water-jacket cooling system only (at 3, 6 and 10 L/min). Moreover, in order to characterize the influence of end-winding channel flow rate on the winding temperature independently from the water-jacket flow rate, we decided to change the flow rate of the end-winding channel while keeping the same water-jacket flow rate. As a result, we had a total of 12 tests as shown in the test matrix from Table 6.

Table 6 – Test matrix for motor cooling experiments

Test number	Water-jacket flow rate [L/min]	End-winding channel flow rate [L/min]
Test 1	3	None
Test 2	6	None
Test 3	10	None
Test 4	3	3
Test 5	3	6
Test 6	3	10
Test 7	6	3
Test 8	6	6
Test 9	6	10
Test 10	10	3
Test 11	10	6
Test 12	10	10

The first step of the experimental procedure was to stabilize the WEG coolant temperature in the bath at 65°C while running the pump. The power supplies are off for this first step. As the stator was insulated using fiberglass, the thermocouples were all

indicating a temperature around 65°C when we had reached steady state. Steady state was defined as the state for which thermocouple temperature change was less than ± 0.1°C for a 10 min time interval. This ± 0.1°C corresponds to the maximum thermocouple calibration uncertainty.

Once the temperature reached steady state, we turned on the power supplies at a fixed current of 160 A. We were recording the transient time frame only for test 2, 7, 8 and 9 for a fixed flow rate of 6 L/min in the Water-Jacket. For all the other tests we were just monitoring the transient temperatures in a plot window of the LabVIEW program. Once we reached steady state for the end-winding temperatures, we recorded 120 samples with a 1 second time step. After recording the 120 samples we moved to the next test by changing the flow rates accordingly. As the flow was changed, so did the temperatures. Therefore, when moving from one test to another we had to wait for the new temperature steady state. The ambient temperature in the lab was not monitored as we had fully insulated stator. Therefore, the ambient temperature for our motor was considered to be the inlet temperature of the coolant.

4.3 Test results and discussion

In this section, the results of our experiments are provided from test 1 to test 12 at steady state. As the main objective of this test is to compare the impact of the new end-winding channel on the end-winding temperatures, the temperatures of interest for this section are the temperature from the 32 thermocouples in the rear end-windings shown in Figure 34.

4.3.1 Steady state temperature results

In the rear end-windings, the temperatures are measured at 4 different surfaces as defined in 4.2.4. and the kth surface is defined such that $k \in$ $\{Rear\ End\ Outer, Rear\ End\ Inner, Rear\ End\ Top, Rear\ End\ Inside\}$. At the kth surface, we have $N = 8$ sections and at each section noted i, we take $n = 120$ temperature samples. As a result, we note T_{ij}^k the jth temperature measurement at the ith section of the kth surface of the end-windings. $\overline{T_i^k}$ is defined as the mean temperature of the n samples at the ith section of the kth surface of the end-windings. The temperatures $\left[\overline{T_i^k}\right]$ are computed for each test in Table 6 and the results are shown in Figure 37.

For any surface k, the graphs show that, as we are increasing the flow rate in the water-jacket without end-winding channel, the end-winding temperature decreases. Indeed, the heat absorbed by the fluid is proportional to the mass flow rate of the fluid in the water-jacket. We observed the same phenomenon when the end-winding channel are connected, however, the impact of the water-jacket flow rate on the end-winding temperature decrease is less significant in this case. Some part of the heat produced by the rear end-windings is directly absorbed by the end-winding channel. However, this does not necessarily mean that the overall impact of the water-jacket mass flow rate on the winding temperatures is less significant. Indeed, the slot-winding temperatures are probably still significantly impacted by the water-jacket flow rate. However, we did not have measurements inside the slot-windings to assess how the slot-winding temperatures were affected when including the end-winding channel cooling system.

(a) Rear End Outer

(b) Rear End Inner

(c) Rear End Top

(d) Rear End Inside
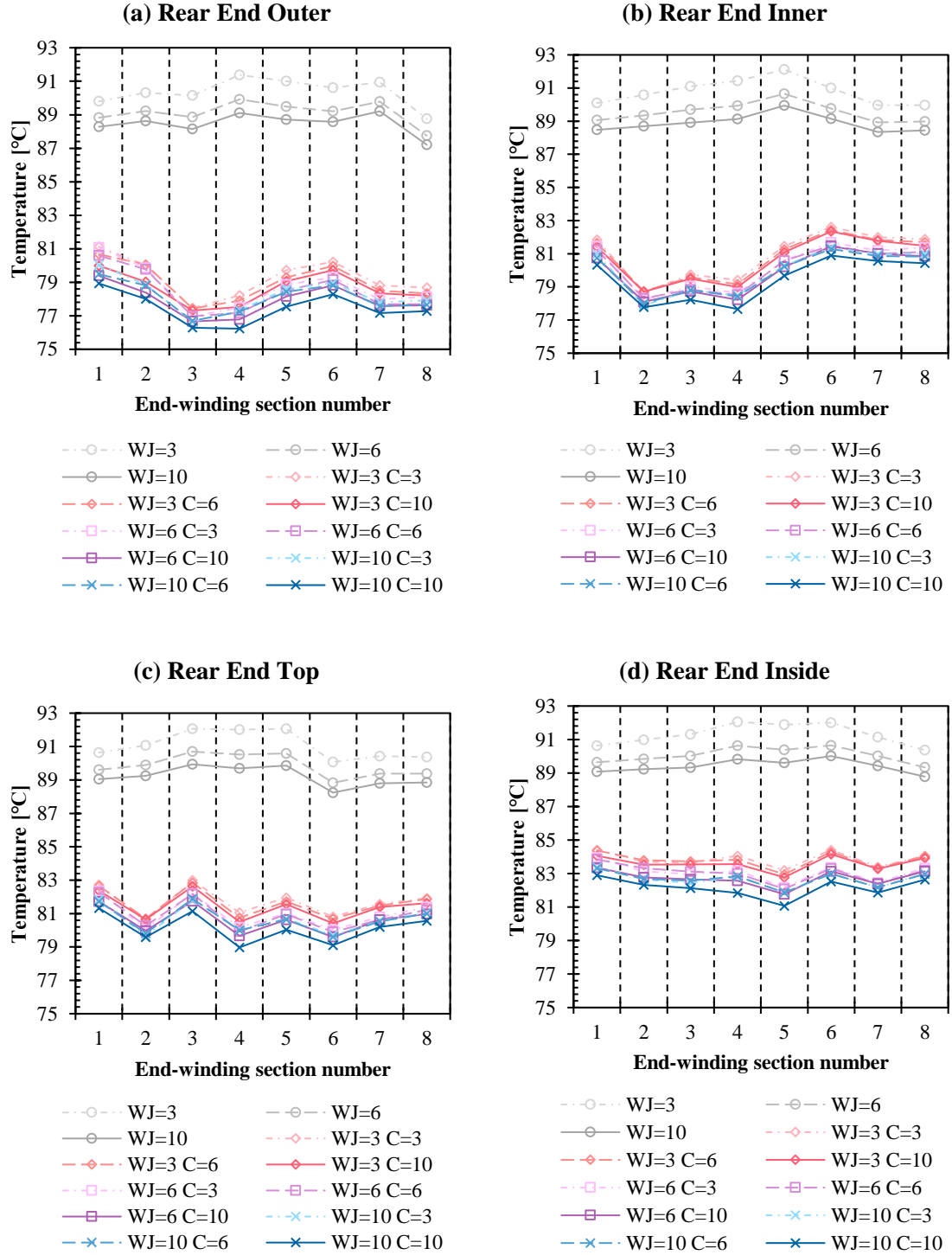
Figure 37 – Steady state mean temperatures in the rear end-windings for each end-winding section and each flow rate (L/min) in the water-jacket ("WJ") and end-winding channel ("C"). For example, "WJ=3 C=3" is equivalent to: Water-jacket flow rate = 3 L/min and End-winding channel flow rate = 3 L/min.

When using the end-winding channel, one could expect that the end-winding temperatures at each surface would gradually increase as we are far from the inlet where we have the lowest coolant temperature. However, for a fixed flow rate through the water-jacket and end-winding channel, the temperature distribution is not conservative when moving from one section to another. For example, we have the highest top surface temperature in section 3 (from graph (c)) whereas we have the lowest outer surface temperature in the same section (from graph (a)). Moreover, the maximum fluid temperature difference between the outlet and inlet of the end-winding channel is lower than 1°C while the end-winding temperature difference between one section and another in Figure 37 can be higher than 2°C. Therefore, the temperature variations from one section to another are not directly due to the coolant temperature increase as it flows around the end-windings. Additionally, the temperature variation from one section to another looks almost random. The source of this variation could then be due to the uncertainty of the temperature measurements. However, the maximum combined uncertainty $u_c(\overline{T_i^k})$ (see definition in APPENDIX A.1) for $\left[\overline{T_i^k}\right]$ temperatures is lower than 0.2°C which is much lower than the observed temperature difference in Figure 37. Nevertheless, many sources of errors were not considered in this uncertainty analysis as they were difficult to quantify.

The first source of error could be the randomness of the wire distribution in the end-windings coupled with the thermocouple location. Indeed, we can observe on Figure 34 that the temperature on the top surface is not uniform. For example, if we place the thermocouple at the top of one wire or between two wires this will already affect the effective measured temperature. Moreover, we may not have placed the thermocouple for one surface at the exact same location from one section to another, especially for the outer

surface which was difficult to access. A second source of error is the shape difference between one end-turn from two different sections. Finally, a third source of error could be the thickness of the highly conductive epoxy between the thermocouple and the end-windings. This thickness is inevitably changing from one thermocouple to another.

Due to the randomness of this temperature variation from one section to another, we have decided to take the arithmetic average of all section temperatures for each surface instead of the individual temperatures. This results in only one mean temperature $\overline{T^k}$ per surface k. The resulting temperature values for each flow rate in the water-jacket and end-winding channel are shown in Figure 38. The error bars represent the extended combined uncertainty $U_c(\overline{T_k})$ as defined in APPENDIX A.1.

In Figure 38, we can better compare the temperatures at each surface of the end-windings. When the end-winding channel is not used, the temperature values from one end-winding surface to another are close. Indeed, without end-winding channel, the external surfaces are directly in contact with air which has a very low thermal conductivity. Thus, the heat flow from each end-winding surface to the ambient air is close to zero at steady state.

As expected, when the end-winding channel is used, the inside temperatures are the highest. Indeed, the distance between the inside surface and the channel wall is higher than for other surfaces, leading to a higher thermal resistance. Besides, for a fixed water-jacket flow rate, the end-winding temperature difference for a 3 L/min flow rate and a 10 L/min flow rate in the end-winding channel is less than 1°C. Thus, we are able to significantly

reduce the end-winding temperatures even at lower flow rate, resulting in lower hydraulic power requirement.
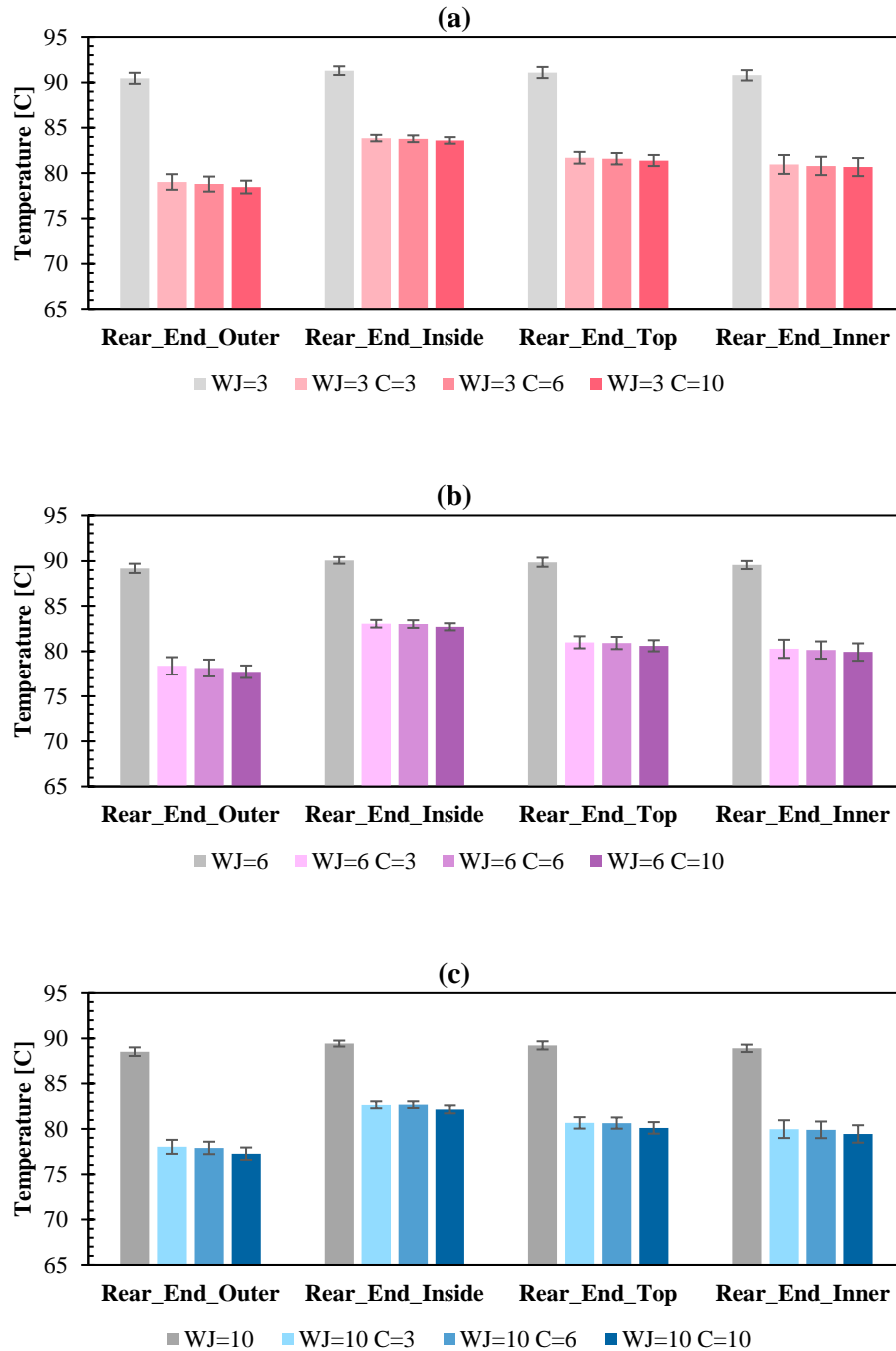
Figure 38 – Mean end-winding temperature on the outer, inside, top and inner surfaces for a water-jacket flow rate of 3 L/min (a), 6 L/min (b) and 10 L/min (c).

To quantify the effective performance of the end-winding channel cooling system, a temperature rate of decrease ξ^k has been defined for each surface k of the end-windings. The definition of ξ^k is given in (29).

$$\xi^k = 1 - \frac{T^k_{WJ+EWC} - T_{fluid,WJ}}{T^k_{WJ} - T_{fluid,WJ}} \tag{29}$$

Where: T^k_{WJ+EWC} is the temperature of the kth surface when using both the water-jacket and end-winding channel cooling systems, T^k_{WJ} is the temperature of the kth surface when using the water-jacket cooling system only and $T_{fluid,WJ}$ is the fluid temperature at the inlet of water-jacket.

The values of ξ^k at each flow rate of the water-jacket and the end-winding channel are shown in Figure 39. For each value error bars are given. These error bars represent the extended uncertainty $U_c(\xi^k)$ using propagation of uncertainty from temperature measurements. This process is developed in APPENDIX A.1.

The maximum value of ξ is 47% while the overall lowest value is 28%. However, this lower value is measured on the inside surface which, again, is far from the end-winding channel wall compared to the other surfaces. Therefore, if we only consider the closest end-winding surfaces to the channel wall, namely "outer", "inner" and "top" surfaces, the lowest ξ is 35%. These numbers demonstrate a very good cooling capability of the end-winding channel.
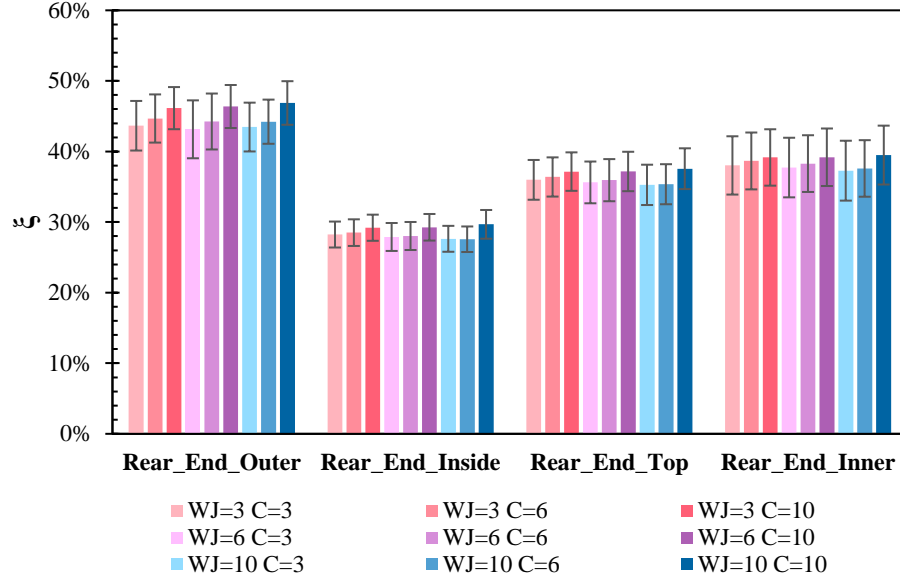
Figure 39 – ξ values for each end-winding section k and each flow rate (L/min) in the water-jacket ("WJ") and end-winding channel ("C").

This high rate of temperature decrease is due to two major factors. The first factor is the coolant proximity to the end-windings. This coolant has a temperature of 65°C at the inlet and the temperature difference between the inlet and outlet is negligible in our experiments (less than 1°C at the lowest flow rate). Therefore, considering the Newton's law of cooling given in (5), the temperature difference between the end-winding surface and the coolant is maximized. Moreover, the U-shape of the channel maximizes the area of the heat transfer. The remaining parameter which represents the second major factor is the overall heat transfer coefficient U between the end-winding external surfaces and the coolant. This parameter is the most critical for our cooling system. While the low thermal conductivity of the ULTEM material is limiting the maximum value of U, the highly conductive silicone compound used at the interface between the channel wall and the end-windings plays a key role in improving the value of U. Without this silicone compound,

the airgap between the channel wall and the end-windings would drastically reduce the performance of the cooling system.

As a reminder, the end-winding channel is only used at the rear end-windings which means the front end-winding does not have any direct cooling system. Assuming the end-winding channel system is also integrated in the front end-winding, we would probably have the same rate of decrease for the front of the end-windings. Reducing the overall winding temperature for the same electric power input means that the electric motor power density is increased. Indeed, the fixed maximum temperature of the winding will be reached for a higher electric power input if the end-winding channel is used on both the front and rear end-windings.

This first prototype was supposed to be a proof of concept constrained by time and resources as developed in 4.1.2. Many improvements could be made to this design to increase U. By using another manufacturing process of the end-winding channel, the thickness of the channel wall could be reduced. ULTEM 9085 has a very high strength compared to other traditional polymers. Consequently, the wall thickness could be reduced without compromising the capability of the channel to withstand the internal pressure. U could be also improved by using a material with higher thermal conductivity. We assumed that using a metallic material like aluminum would present a risk of short-circuit as the end-windings are very close to the channel wall. However, further investigation is needed, and it may be possible to use a metallic material by ensuring a minimum distance between the wall and the end-windings. The combination of a lower wall thickness and use of metallic material for the channel could lead to even much better cooling performance.

4.3.2 Heat balance

The heat absorbed by the fluid note q_{fluid}, in the water-jacket or the end-winding channel, can be defined by:

$$q_{fluid} = \dot{m}c_{p\,fluid}(T_{inlet} - T_{oulet}) \tag{30}$$

Where $\dot{m}$ is the fluid mass flow rate, $c_{p\,fluid}$ is the specific heat of the fluid, T_{inlet} and T_{outlet} are the mean temperature of the fluid at the inlet and outlet of the cooling system, respectively.

The temperatures T_{inlet} and T_{oulet} and their difference ΔT are given in Table 7 for both the water-jacket and the end-winding channel at different flow rates (test 4 to 12).

Table 7 – Temperature at the inlet and outlet and the resulting ΔT for both the water-jacket and the end-winding channel from test 4 to 12.

	Water-jacket			End-winding channel		
	T_{outlet} [°C]	T_{inlet} [°C]	ΔT [°C]	T_{outlet} [°C]	T_{inlet} [°C]	ΔT [°C]
WJ=3 C=3	64.0	66.2	-2.2	63.9	64.4	-0.4
WJ=3 C=6	64.1	66.3	-2.2	64.4	64.8	-0.3
WJ=3 C=10	64.3	66.5	-2.1	64.8	65.0	-0.3
WJ=6 C=3	64.6	65.6	-1.0	64.0	64.6	-0.5
WJ=6 C=6	64.5	65.6	-1.1	64.4	64.8	-0.4
WJ=6 C=10	64.8	65.9	-1.1	64.8	65.1	-0.2
WJ=10 C=3	64.8	65.5	-0.7	64.2	64.6	-0.4
WJ=10 C=6	65.0	65.7	-0.7	64.7	65.0	-0.3
WJ=10 C=10	65.0	65.6	-0.6	64.9	65.1	-0.2

Overall, the values of ΔT are low: less than 1°C for the end-winding channel and less than 3°C for the water-jacket. This is due to a low value of the total power input that we are using (around 530 W). In the real application this value can go up to the maximum power of the motor, 80 kW (see Table 1). This is more than 100 times the total power input from our experiments, which means the ΔT value can go much higher than what we have for these experiments.

Considering that we are measuring the volumetric flow rate instead of the mass flow rate and as our fluid is incompressible, q_{fluid} can be expressed as a function of the fluid density ρ_{fluid} which yields:

$$q_{fluid} = \rho_{fluid} c_{p_{fluid}} \dot{V}(T_{inlet} - T_{oulet}) \tag{31}$$

q_{fluid} has been computed for both the water-jacket and the end-winding channel for each different flow rates (test 4 to 12). As we have only DC current in our experiments all the electric power is converted into heat following equation (1). Consequently, q_{fluid} can be compared to the total electric power from the power supplies to know which part of the heat is absorbed by the fluid. The results of this comparison are given in Figure 40. The error bars correspond to the sum of extended uncertainty $U_c(q_{fluid})$ for the water-jacket and end-winding channel as defined in APPENDIX A.3   Heat   balance uncertainty
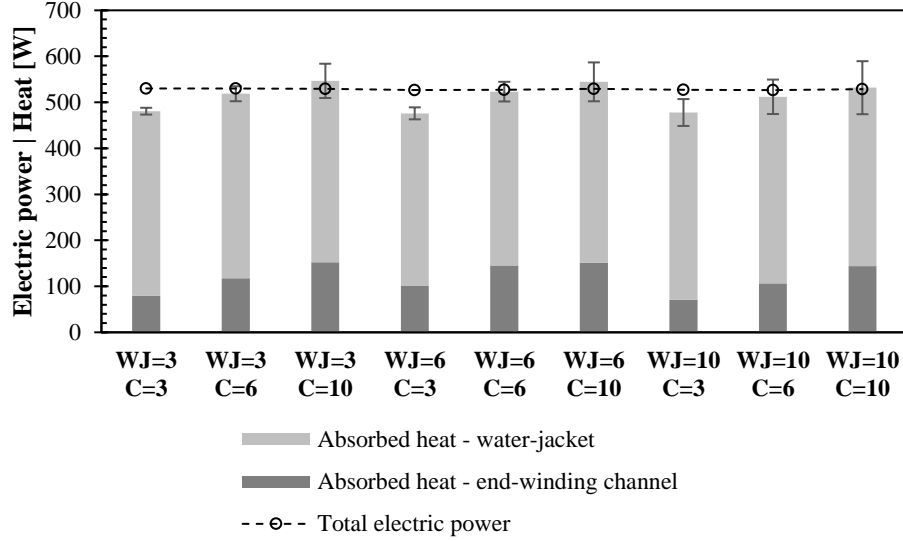
Figure 40 – Absorbed heat in the water-jacket and the end-winding channel compared to the total electric power input at each flow rate (L/min) in the water-jacket ("WJ") and end-winding channel ("C").

If the motor was perfectly insulated when using the fiber glass for the experiments, all the heat generated by the windings should be absorbed by the fluid based on heat flow conservation. However, in Figure 40, for a fixed flow rate of 3 L/min in the water-jacket, the total heat absorbed by the fluid is lower than the total heat input by around 9%. A reasonable explanation for this gap would be heat dissipation to ambient air. Indeed, the thermal insulation of the motor with fiber glass is not perfect. As the water-jacket flow rates increases, the cooling systems are able to absorb more heat as equation (31) suggests it. However, at the highest flow rates for the water-jacket, the calculated absorbed heat is higher than the total heat input of the system. This is probably due to measurement uncertainty. Indeed, the higher the total flow rate, the lower the ΔT and the higher the error. This is the reason why the size of the error bars grows as we are looking at higher flow rate in Figure 40. Moreover, in the uncertainty analysis for $U_c(q_{fluid})$, we only consider the

uncertainty of the thermocouples and the flow sensor; however, other parameters must be affecting the temperature measurements, such as the height of the thermocouple in the tube, the local flow turbulence, tiny air bubbles stuck in the T fittings. Consequently, the total uncertainty is probably higher $U_c(q_{fluid})$. Therefore, the exact value of the absorbed heat should be carefully interpreted.

The heat absorbed by the fluid in the end-winding channel represents a minimum of 15% and a maximum of 28% of the heat absorbed by the fluid in the water-jacket. The minimum is reached when the flow rate in the water-jacket is maximum and the flow rate in the end-winding channel is minimum ("WJ=10, C=3") whereas the maximum is reached when the flow rate in the water-jacket is minimum and the flow rate in the end-winding channel is maximum ("WJ=3, C=10"). From the value of the volume ratio $\alpha = 62$ % from (11), we can deduce that the total power generated at the rear end-windings is about 19 % of the total power input. Consequently, if $\dot{V} \geq 6$ L/min in the end-winding channel and for any other tested flow rate in the water-jacket, the end-winding channel cooling system is able to absorb all the heat from the end-windings which is exactly what it was meant for. Again, improvements in the material and wall thickness of the end-winding channel could allow to further increase this performance. Different flow configurations could also be investigated to optimize this cooling system.

4.4   End-winding channel CFD model

In order to predict the global performance of the motor with this new end-winding channel cooling system and optimize its design, we must integrate the end-winding channel in our LPTN model from CHAPTER 3. The first step of the process is to derive the heat

transfer coefficient h_{EWC} characterizing the convective heat transfer between the fluid and the channel wall. As we do not have temperature measurements at the wall in contact with the fluid, we need to compute h_{EWC} using a CFD model of the channel fluid domain. The CFD model and the results for h_{EWC} are presented in the following sections.

4.4.1   CFD model setup

4.4.1.1   Geometry

The end-winding channel fluid domain only was used in the CFD model. This fluid domain is shown in   Figure 41. The cross section of the fluid domain has the same dimension as the internal U-shape from Figure 25. The flow is considered as a turbulent flow (detailed explanation in the following paragraphs). Therefore, the entrance length $L_{entrance}$ was chosen to be 10 times the inlet tube inner diameter D_{inlet}. This rule for the entrance length allows to have a fully developed flow before entering the U-shape channel.
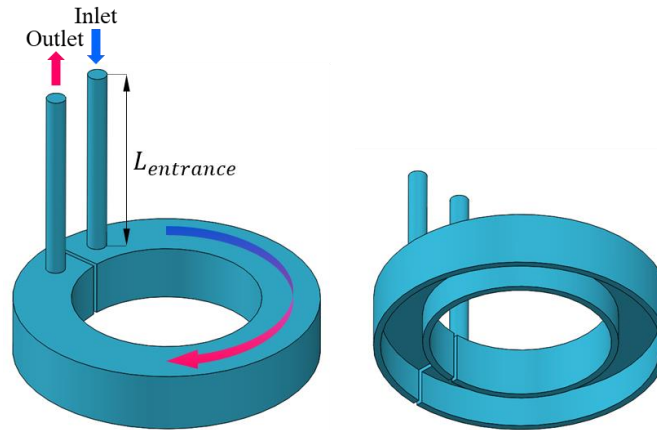
Figure 41 – CFD model fluid domain geometry

4.4.1.2   Physical model

The final version of the CFD model was created using ANSYS 2020 R2 software with ANSYS Meshing and Fluent packages. As we have a liquid coolant, the fluid is considered as incompressible. Before selecting the viscous model for this study, we calculated the value of the Reynolds number Re for the three different flow rates tested in our experiments (3 L/min, 6 L/min and 10 L/min) and at two different areas of the end-winding channel: at the inlet tube cross section and in the U-shape channel cross section. Re is defined as follows:

$$Re = \frac{\rho_{fluid} u D_h}{\mu} \tag{32}$$

Where ρ_{fluid} is the WEG density, u is the fluid velocity, μ is the fluid dynamic viscosity and D_h is the hydraulic diameter.

WEG (50%-50% by volume of water and ethylene glycol) properties for a temperature of 65°C are given in Table 8 [65]. These values are deduced from the graphs in Figure 48 from Water Ethylene Glycol properties.

Table 8 – WEG with 50% volume of water properties at 65°C [65].

WEG property	Value
Density [kg/m^3]	1048
Specific heat [J.kg^{-1}.K^{-1}]	3449
Thermal conductivity [W.m^{-1}.K^{-1}]	0.390
Viscosity [cP]	1.319

The velocity u in equation (32) is derived from the volumetric flow rate divided by the cross-section area of either the tube or the U-shape channel. D_h is equal to the diameter for the tube section. For the U-shape channel section, $D_h = 4P_{EWC}/A_{EWC}$ where P_{EWC} and A_{EWC} are the perimeter and the area of the U-shape channel respectively. The different values of the geometric parameters are given in Table 9.

Table 9 – Geometric parameters of the end-winding channel fluid domain used in the CFD model.

Parameter	Value
P_{EWC} [mm]	203
A_{EWC} [mm^2]	763
D_h | U-shape channel [mm]	15.0
D_h | Inlet tube [mm]	12.7
$L_{entrance}$ [mm]	127

The Re values at three different flow rates and for both the inlet tube and U-shape channel are calculated using equation (32). The Re values and their associated velocities are reported in Table 10. The transition from laminar to turbulent flow in pipes is usually characterized by a critical Reynolds number Re_{crit}. In straight pipes, $Re_{crit} \approx 2100$ but for the curved U-shape this Re_{crit} is higher according to helical pipe correlation [59]. From the Re values in Table 10, the flow in the inlet tube can be always considered as turbulent while the flow in our channels is always laminar if we consider the Re_{crit} due to the curved pipe. As we have a turbulent regime in our inlet and outlet pipe and considering the complexity of the U-shape cross section of the channel, a turbulent model was used for our CFD model.

Table 10 – Velocity and *Re* values at the inlet tube and U-shape channel for different flow rates.

Flow rate [L/min]	Inlet tube		U-shape channel	
	u [m/s]	*Re*	u [m/s]	*Re*
3.0	0.395	3985	0.065	782
6.0	0.789	7970	0.131	1563
10.0	1.316	13284	0.218	2606

After comparing different types of turbulent model available in ANSYS Fluent by looking at the different residuals and temperature, pressure and mass flow convergence, we decided to use the SST k-ω model developed in [60] where k is the turbulent kinetic energy and ω is the specific rate of dissipation of k into internal thermal energy. This turbulence model is solving for the Reynolds-Average Navier-Stokes (RANS) equations describing turbulent flow as well as the transport equation for k and ω as defined in [60]. In addition to the RANS equations, we are also solving for the energy equation in order to compute the temperature distribution in the fluid and derive h_{EWC}.

4.4.1.3   Boundary conditions

At the inlet, we have a uniform velocity boundary condition. The value of this velocity can be found in Table 10 under "Inlet tube". The outlet is a fixed pressure boundary condition at 0 Pa. All the other external surfaces are considered as 1 mm thick walls with no-slip condition. When considering a roughness height equal to half of a ULTEM filament width, we did not have a significant impact on h_{EWC} value. Therefore, we decided to simplify the model and have no roughness at the wall.

We assumed the heat transfer on outside surfaces (shown in grey in Figure 42) to be negligible compared to the inside surfaces in direct contact with the end-winding (shown in red Figure 42). Therefore, all walls were considered as adiabatic except for the outer, inner, and top side of the channel as shown in Figure 42. A constant heat flux is applied at these three surfaces. The applied heat flux q''_{wall} value is equal to the heat absorbed by the fluid given in Figure 40 for each flow rate, divided by the total combined area of the outer, inner, and top surfaces. We decided to take the absorbed heat value for a fixed water-jacket flow rate of 10 L/min. The resulting heat flux values are 1861 W/m^2, 2800 W/m^2, and 3787 W/m^2 for an end-winding channel flow rate of 3 L/min, 6 L/min and 10L/min respectively.
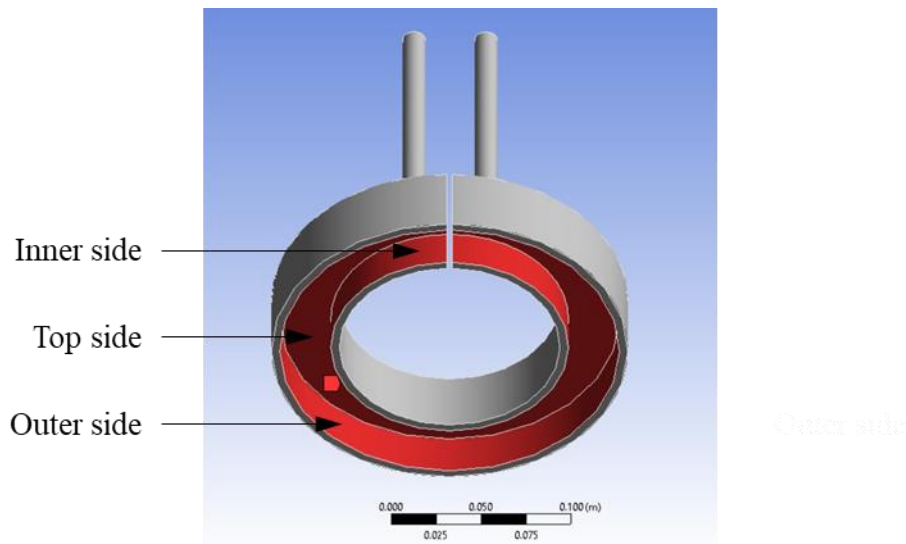
Figure 42 – Channel surfaces considered for the heat transfer between channel walls and the end-windings.

4.4.1.4   Meshing

The fluid domain mesh had a total of ~955,000 cells. Pictures of the mesh are shown in Figure 43. The base size of the mesh is 2 mm, and the boundary layer has 7 layers for a total thickness of 1.3 mm. The thickness and the number of cells was chosen after a few

iterations to obtain a convenient value of y+ lower than 4 at the wall and a fine mesh in the outer and inner side of the channel. Indeed, we wanted to make sure we did not have significant temperature or velocity gradients between two consecutive cells in the viscous sublayer. The final mesh was chosen after a mesh independence study based on the computed heat transfer coefficient h_{EWC} and the pressure drop between the inlet and the outlet. The results of this mesh independence study are given in Figure 44.
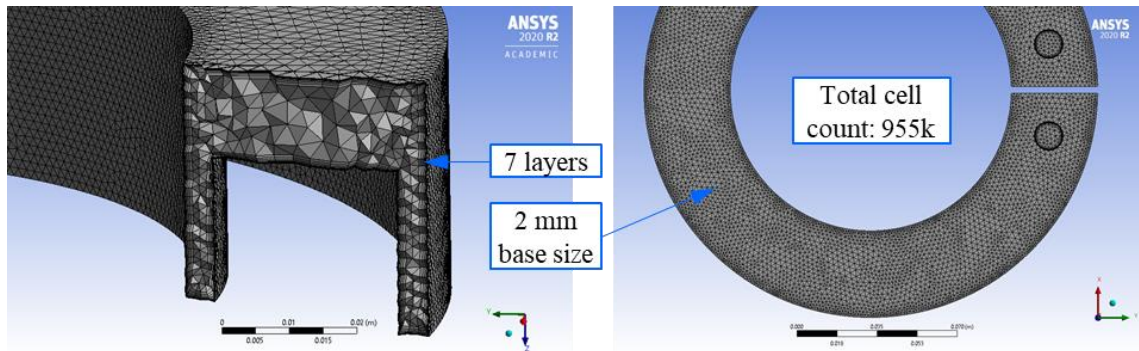
Figure 43 – Fluid domain mesh
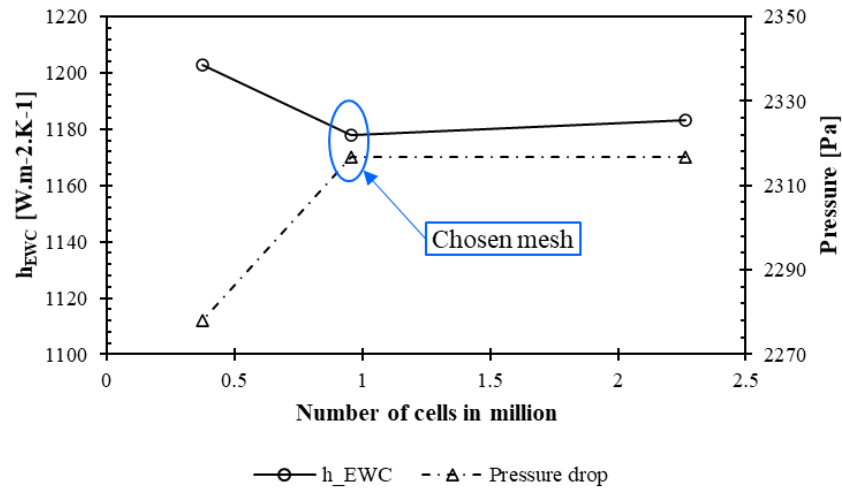
Figure 44 – Mesh independence study, h_{EWC} and total pressure drop with respect to the total number of cells in the CFD model.

4.4.2   CFD results

The steady-state simulations of the end-winding channel fluid domain were performed for a flow rate of 3 L/min, 6 L/min and 10 L/min. The wall temperatures as well as the velocity streamlines for a flow rate of 10 L/min in the end-winding channel obtained from the steady-state simulation are shown in Figure 45. In Figure 45 (a), the external wall temperature is almost equal to the fluid average temperature as we have considered these walls to be adiabatic. However, the inside, outer, inner, and top walls show a much higher temperature increase especially on the outer wall as we get closer to the outlet of the channel.

(a) Wall temperatures   (b) Velocity streamlines
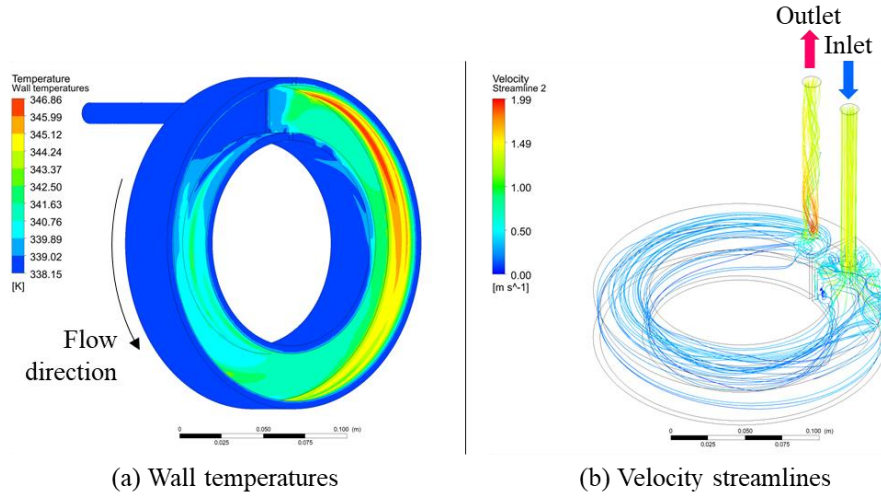
Figure 45 – Wall temperatures (a) and Velocity streamlines (b) from steady-state simulation of the end-winding channel fluid domain for a flow rate of 10 L/min.

From the temperature results from the simulation the average temperature $\overline{T_{fluid}}$ was defined as follows:

$$\overline{T_{fluid}} = \frac{\overline{T_{inlet}} + \overline{T_{outlet}}}{2} \tag{33}$$

Where $\overline{T_{inlet}}$ and $\overline{T_{outlet}}$ are the mass flow weighted average temperature at the inlet and the outlet, respectively.

The heat transfer coefficient h_{EWC} was computed using ANSYS CFD-Post using the definition from equation (34)(41).

$$h_{EWC} = \frac{q''_{wall}}{\overline{T_{wall}} - \overline{T_{fluid}}} \tag{34}$$

Where T_{wall} is the area weighted average temperature at the inside surface (combination of the outer, inner and top surface from Figure 42).

We have also computed the equivalent heat transfer coefficients at each inside surface: $h_{EWC_{outer}}$, $h_{EWC_{inner}}$, and $h_{EWC_{top}}$. The only difference in the definition of these individual heat transfer coefficients is that $\overline{T_{wall}}$ is defined as the area weighted average temperature for each individual surface instead of the total inside surface. The values of each heat transfer coefficient are given in Table 11.

Table 11 – Heat transfer coefficients derived from CFD steady-state simulation for three different flow rates.

Flow rate [L/min]	h_{EWC} [W.m^{-2}.K^{-1}]	$h_{EWC_{inner}}$ [W.m^{-2}.K^{-1}]	$h_{EWC_{outer}}$ [W.m^{-2}.K^{-1}]	$h_{EWC_{top}}$ [W.m^{-2}.K^{-1}]
3.0	546	612	413	742
6.0	839	1043	639	1042
10.0	1177	1472	889	1483

For a flow rate of 10 L/min, $h_{EWC} = 1177\ W.m^{-2}.K^{-1}$. As a comparison, the water-jacket heat transfer coefficient h_{WJ} for the same flow rate is $1428\ W.m^{-2}.K^{-1}$. The cross-sectional area of the end-winding channel A_{EWC} is close to that of the water-jacket channels, and the curvature radius is also similar. This would suggest that h_{EWC} and h_{WJ} are close. However, the water-jacket is made of aluminum which has a much higher thermal conductivity than ULTEM. Therefore, h_{EWC} must be slightly lower than h_{WJ} and this is exactly what we observed from our results. Consequently, h_{EWC} computed from our CFD model seems consistent.

4.5 End-winding channel LPTN model

In order to predict the impact of the end-winding channel on the performance of the end-winding channel, and possibly compare it to other cooling system, we must integrate the end-winding channel component into our LPTN model from CHAPTER 3. This integration includes creating an equivalent resistance network representing the end-winding channel and calibrating the parameters of the end-winding channel resistances to match the experimental results. These steps are presented in the section below.

4.5.1 End-winding channel resistance network

The end-winding channel equivalent network is represented by three resistances, R_{outer}, R_{inner} and R_{top} as shown in Figure 46. These resistances connect the nodes from each sides of the end-windings (T_{outer}, T_{inner} and T_{top}) to the fluid node $\overline{T_{fluid}}$ as defined in (33). Each resistance R_i, for $i \in \{outer, inner, top\}$, is a combination of conduction and contact resistances in series from T_i to $\overline{T_{fluid}}$. G_{1_i} and G_{2_i} are the thermal contact

91

conductance at the interfaces End-windings | Potting and Potting | Channel wall, respectively. These thermal contact conductances account for any air bubbles trapped between the end-windings and the potting (silicone compound) due to the surface roughness. k_{pot} is the thermal conductivity of the potting material, 3.5 W.m^{-1}.K^{-1}, and k_{ULTEM} is the thermal conductivity of ULTEM 9085 equal to 0.25 W.m^{-1}.K^{-1} for temperatures around 90°C (maximum temperature of the end-windings in our experiments) according to the experimental data from [61]. h_{EWC_i} is the heat transfer coefficient for surface i. The values for h_{EWC_i} are taken from the CFD results given in Table 11. The areas A_{outer}, A_{inner} and A_{top} corresponds to the area of the surfaces represented in red in Figure 42. In Figure 46, the thickness of the potting and channel wall are not representative of the real dimensions. In the real motor assembly, the distance between the channel wall and the end-windings is small enough to consider that the change in area from the wall to the end-windings is negligible. Eventually, L_{pot_i} and $L_{channel}$ are the thicknesses of the potting layer and the channel wall, respectively. $L_{channel}$ is equal to 1 mm. However, L_{pot_i} is almost impossible to measure accurately as the end-windings are not perfect flat surfaces as shown in Figure 30. For instance, on the outer side, the winding coming from the slot are curved to reach to top surface and then go back to the next slot. Therefore, the potting thickness is a function of both axial and tangential coordinates and can differ from one surface to another. Besides, the equivalent thickness of the potting may be different from one side to another, hence the L_{pot_i} dependence on the surface i.
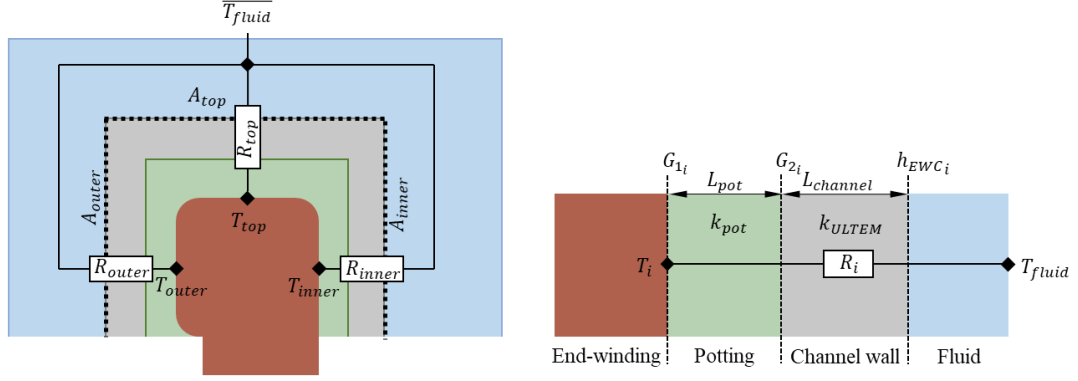
Figure 46 – End-winding channel equivalent resistance network

R_i can be defined as an equivalent resistance of individual resistances in series corresponding to each layer between the fluid and the windings:

$$R_i = \frac{1}{A_i \times G_{1_i}} + \frac{L_{pot_i}}{A_i \times k_1} + \frac{1}{A_i \times G_{2_i}} + \frac{L_{channel}}{A_i \times k_2} + \frac{1}{A_i \times h_{EWC_i}} \qquad (35)$$

In Motor-CAD® LPTN, the end-windings are defined using cuboids as explained in the 3.1.2.4. section. Consequently, the resistance R_{top} must be divided into n_{cub} (number of cuboids) resistances, with the same value R'_{top}, in parallel with one extremity connected to the cuboid node at the end-winding top surface and the other connected to the $\overline{T_{fluid}}$ node. As all resistances R'_{top} are in parallel, and the only changing parameter from R_i to R'_{top} is the effective surface A_i, we have $R'_{top} = R_i \times n_{cub}$. All the resistances of the end-winding channel resistance network are now defined and can be integrated inside the LPTN shown in Figure 10.

In the expressions of R_{inner}, R_{outer}, and R'_{top}, the variables G_{1_i}, G_{2_i} and L_{pot_i} are unknown. Therefore, we need to calibrate these resistances using the temperature results from our experiments.

4.5.2   LPTN calibration

The calibration consists of changing the values of our unknown in the expression of the end-winding channel network resistances to minimize the error ε between the LPTN and experimental temperatures. The definition of this error was based on previous calibration work from [62] and is given below:

$$\varepsilon = \sum_{i \in \{inner, outer, top\}} \frac{\left|T_{i|Experiments} - T_{i|LPTN}\right|}{T_{i|Experiments}} \tag{36}$$

Where $T_{i|Experiments}$ is the value at the temperature node T_i from experiments and $T_{i|LPTN}$ is the value at the temperature node T_i from the LPTN.

As can be noticed, we only have 3 node values for the calibration, while we have 9 unknowns if we consider that G_{1_i}, G_{2_i} and L_{pot_i} can have a different value from one surface i to another. Therefore, for the calibration process, we decided to simplify the problem in order to have only 3 unknowns. For this, we considered an equivalent thermal resistance R_{eq_i} at each surface i such that:

$$R_{eq_i} = \frac{L_{eq_i}}{A_i \times k_1} = \frac{1}{A_i \times G_{1_i}} + \frac{L_{pot_i}}{A_i \times k_1} + \frac{1}{A_i \times G_{2_i}} \tag{37}$$

Where L_{eq_i} is the equivalent thickness of the potting material including the thermal contact conductances.

The calibration was conducted using an optimization script in Python with the Sequential Least Square Quadratic Programming (SLSQP) constrained optimization algorithm. The calibration process using this Python script is shown in Figure 47. The values of $\{L_{eq_i}\}$ are changed at each step of the optimization. The lower and upper bounds for the $\{L_{eq_i}\}$ are 1.5 mm and 100 mm, respectively. Then, these values are loaded in Motor-CAD®. A steady-state simulation is performed to obtain the new temperatures $\{T_i\}$ from the LPTN. These new values are used to compute the new error ε. This loop stops once the error is lower than 0.001 or when the number of steps n_{step} is greater than 200. The maximum number of steps n_{step} is fixed to 200. This calibration algorithm is repeated for each flow rates so that the error is minimized for the all the investigated flow rates in the water-jacket and end-winding channels.
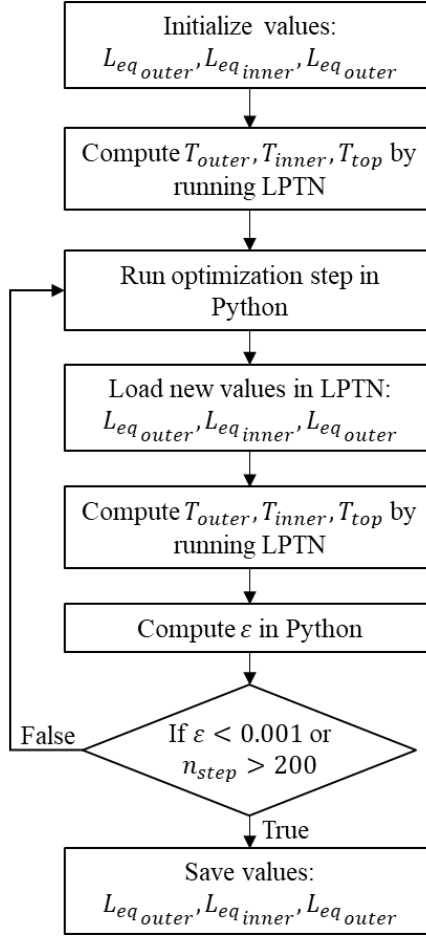
Figure 47 – Calibration algorithm using LPTN in Motor-CAD® and the Python script.

After performing the calibration, the maximum temperature difference between the experimental results and the LPTN results is 1.06°C (considering all flow rates in the end-winding channel and the water-jacket). This shows an excellent agreement between the LPTN model and the experiments. The values of $\left\{L_{eq_i}\right\}$ obtained after performing the calibration are given in Table 12. These values do not represent real dimensions as one length L_{eq_i} includes the resistances associated with G_{1_i} and G_{2_i}. If we want to know the individual values, we must have experimental values for other nodes in the LPTN. However, assuming we have the same average potting thickness L_{pot} for each surface i,

we can have an estimation of the equivalent thermal contact conductance G_{eq_i} defined as the combination of G_{1_i} and G_{2_i} associated resistances:

$$G_{eq_i} = \left(\frac{1}{G_{1_i}} + \frac{1}{G_{2_i}} \right)^{-1} \tag{38}$$

By combining equations (37) and (38), the expression of G_{eq_i} becomes:

$$G_{eq_i} = \frac{k_1}{L_{eq} - L_{pot_i}} \tag{39}$$

The value of $L_{eq_{top}}$ is equal to the lower bounds from the calibration which suggest that we have a perfect contact between the top of the end-windings and the channel. This is consistent with the fact that this surface is perpendicular to the applied pressure direction when the end-winding channel was pushed to the end-windings, hence the n/a value in Table 12. We considered then that $L_{pot} = L_{eq_{top}} = 1.50\ mm$. With this consideration, we can use equation (39) to derive the values $G_{eq_{outer}}$ and $G_{eq_{inner}}$ given in Table 12.

Table 12 – Potting equivalent length and thermal contact conductance results from the LPTN calibration.

$L_{eq_{outer}}$ [mm]	$L_{eq_{inner}}$ [mm]	$L_{eq_{top}}$ [mm]	$G_{eq_{outer}}$ [W.m^{-2}.K^{-1}]	$G_{eq_{inner}}$ [W.m^{-2}.K^{-1}]	$G_{eq_{top}}$ [W.m^{-2}.K^{-1}]
16.45	13.33	1.50	234	295	n/a

These thermal contact conductance are low when compared to the thermal contact conductance at the slot-liner (Table 2). The inner and outer surfaces are parallel to the pressure directions when inserting the end-winding channel. Consequently, the potting

material is probably stretched as the channel is pushed to the end-windings, resulting in potential air pocket between the end-windings and the channel as the potting material is pushed away. These air pockets may explain the low thermal contact conductances for the outer and inner side of the channel. These low conductance values have a direct impact on the cooling performance of the end-winding channel. If the potting material was put in the groove of the U-shape channel instead of the end-windings, this should avoid stretching the potting material as we insert the channel and thus, significantly improve the thermal contact between the end-windings and the channel for the outer and inner surfaces.

CHAPTER 5.   CONCLUSION

5.1   Research contributions

The increasing need for higher power density electric motors has led to extensive research on the development of disruptive cooling systems to maximize the heat rejection in these motors. While a significant number of concepts and prototypes for the cooling of the active part of the motor have been developed, the end-winding region of the motor did not receive the same attention in the literature. Thus, we decided to contribute to the research on motor cooling solution for the end-windings. In this work, we proposed an alternative to the existing end-winding cooling systems using the Nissan Leaf electric motor as a reference for the design.

The first part of this thesis is focused on the validation of an LPTN model based on the Nissan Leaf motor. We proposed a detailed comparison of an LPTN model with experimental data for steady-state thermal analysis of the Nissan Leaf motor stator. The maximum temperature difference between LPTN results and experimental temperatures was under 4%. The LPTN model was also compared to an FEA model, with a maximum difference of 2%. End-windings were found to be a critical region in terms of modeling accuracy. In addition to this validation, a sensitivity analysis was conducted for six thermal resistances involved in the LPTN model. Liner contact resistance had the highest influence. Comparing influences of other thermal resistances has shown that creating a very high-power-density electric motor requires having a cooling system in direct contact with the end-windings.

In the second part, the design process of the proposed end-winding channel cooling system based on the Nissan Leaf motor geometry was developed. The different challenges in the fabrication of the end-winding channel were highlighted, especially the sealing of the bottom and top parts of this cooling system. The end-winding channel system was then assembled into the Nissan Leaf motor. Temperatures of the end-windings were measured at different flow rates in the end-winding channel and the water-jacket of the motor. By using the proposed end-winding cooling system and the water-jacket, the end-winding external temperatures were decreased by a minimum of 35% compared to a cooling solution with the water-jacket alone. Therefore, this end-winding channel shows very promising cooling performance for future high power density motor applications. In order to investigate different design parameters of this system and further improve its performances, a CFD model and an equivalent resistance network of the end-winding channel was developed. From the CFD model, the heat transfer coefficient between the channel and the coolant was computed. A heat transfer coefficient of 1177 $W.m^{-2}.K^{-1}$ for a flow rate of 10 L/min was found. Besides, an end-winding channel equivalent resistance network was developed and integrated in our previously validated LPTN model. Eventually, the resistances of the channel network were calibrated, and potting material thickness and contact conductance were analyzed.

5.2 Future work

The results from the experiments in the last part of this thesis have shown that some elements could be improved. The thickness of the channel could be reduced by using a different manufacturing process for the fabrication of the end-winding channel. Other materials could also be investigated as the thermal conductivity of ULTEM is still a

significant constraint to higher heat flow from the end-windings to the channel. Besides, the thermal contact conductance on the inner and outer sides of the end-windings can be further improved. Therefore, the first part of the future work could be to create a design of experiments involving the different critical parameters of the end-winding channel to optimize its cooling performance.

In the second part, the LPTN model could be developed for the full motor. This way, we would be able to compare the end-winding channel to existing end-winding cooling solutions based on the torque versus speed or efficiency map of the motor for a fixed maximum temperature.

APPENDIX A.   UNCERTAINTY ANALYSIS

A.1   Steady-state average temperature uncertainty

The following uncertainty analysis is derived from the average temperature at each end-winding area given in CHAPTER 4. This analysis is based on methods and definitions given in the NASA Measurement Quality Assurance Handbook [63] and the Guide to the expression of Uncertainty in Measurement (GUM) [64].

The average temperature $\overline{T^k}$ of a given end-winding area $k \in \{outer, inner, top, inside\}$ is computed from the average temperatures $\overline{T_i^k}$ measured in each section of the motor $i \in [\![1, N]\!]$ where $N = 8$. Each average temperature $\overline{T_i^k}$ is the mean of $n = 120$ temperature samples T_{ij}^k measured at steady state.

The ith average temperature $\overline{T_i^k}$ value and its associated standard deviation s_i^k are defined in the following equation:

$$\overline{T_i^k} = \frac{1}{n} \sum_{j=1}^{n} T_{ij}^k \tag{40}$$

$$s_i^k = \sqrt{\frac{1}{n-1} \sum_{j=1}^{n} \left(T_{ij}^k - \overline{T_i^k}\right)^2} \tag{41}$$

The standard uncertainty $u(\overline{T_i^k})$ of each derived temperature $\overline{T_i^k}$ is defined as:

$$u\left(\overline{T_i^k}\right) = \frac{s_i^k}{\sqrt{n}} \tag{42}$$

We must add the uncertainty $u(tc_i^k)$ from the thermocouple calibration to $u(\overline{T_i^k})$ to obtain the combined uncertainty $u_c(\overline{T_i^k})$ for the temperature $\overline{T_i^k}$. $u(tc_i^k)$ is the thermocouple calibration uncertainty using a second order curve fit. The values of $u(tc_i^k)$ for are given in Table 13. Therefore, we must divide by the square root of the number of measurements to have the standard uncertainty of the mean which yields:

$$u_c(\overline{T_i^k}) = \sqrt{u\left(\overline{T_i^k}\right)^2 + \left(u(tc_i^k)\right)^2} \tag{43}$$

Table 13 – Thermocouple calibration uncertainty using a reference temperature probe. Calibration is based on a second order curve fit, valid from 20°C to 120°C.

	Thermocouple uncertainty [°C]							
	$i = 1$	$i = 2$	$i = 3$	$i = 4$	$i = 5$	$i = 6$	$i = 7$	$i = 8$
Rear End Outer	0.031	0.030	0.031	0.030	0.030	0.030	0.030	0.029
Rear End Inside	0.030	0.030	0.030	0.031	0.030	0.030	0.030	0.031
Rear End Top	0.029	0.029	0.030	0.030	0.029	0.030	0.029	0.032
Rear End Inner	0.030	0.030	0.029	0.031	0.030	0.035	0.029	0.029

We can now define the kth average temperature $\overline{T^k}$ and its associated standard deviation s^k. The error associated with $\overline{T_i^k}$ mean operation, comes from the error of the temperature measurements T_{ij}^k which are taken from the same thermocouple. However, the error associated with $\overline{T^k}$ mean operation is independent of the measurement error as $\overline{T_i^k}$

values for a given k are taken from different thermocouples. Consequently, we have a definition of $\overline{T^k}$ standard deviation independent of s_i^k.

$$\overline{T^k} = \frac{1}{N} \sum_{i=1}^{n_k} \overline{T_i^k} \tag{44}$$

$$s^k = \sqrt{\frac{1}{N-1} \sum_{i=1}^{N} \left(T_i^k - \overline{T^k} \right)^2} \tag{45}$$

The standard uncertainty $u(\overline{T^k})$ of each derived temperature $\overline{T^k}$ is defined as:

$$u(T^k) = \frac{s^k}{\sqrt{N}} \tag{46}$$

As $\overline{T^k}$ values are derived from the $\overline{T_i^k}$ values we must combined $\overline{T_i^k}$ uncertainty to $u(T^k)$ in order to have the combined uncertainty $u_c(\overline{T^k})$, hence, equation (47):

$$u_c\left(\overline{T^k}\right) = \sqrt{u\left(\overline{T^k}\right)^2 + \sum_{i=1}^{N} u_c\left(\overline{T_i^k}\right)^2} \tag{47}$$

After this, the expanded uncertainty $U_c(\overline{T_k})$ can be derived. Assuming our combined error for $\overline{T^k}$ can be represented by a normal distribution, we can derive the expanded uncertainty with a 95% confidence by having a coverage factor of $k_{cov} = 2$, which yields:

104

$$U_c(\overline{T_k}) = k_{cov} \times u_c(\overline{T^k}) = k\sqrt{u(\overline{T^k})^2 + \sum_{i=1}^{N} u(\overline{T_i^k})^2 + \left(u(tc_i^k)\right)^2} \qquad (48)$$

From equation (48), we can say that the value of $\overline{T^k}$ is a given temperature $\pm U_c(\overline{T_k})$ with a 95% confidence.

A.2   Temperature rate of decrease uncertainty

The temperature rate of decrease ξ^k is derived from $\overline{T^k}$ temperatures and the fluid temperature $T_{fluid,WJ}$. ξ^k is defined in equation (29). As ξ^k is a function of independent measured temperatures, we can define the combined standard uncertainty $u_c(\xi^k)$ as follow:

$$
\begin{aligned}
u_c(\xi^k)^2 = {} & \left(\frac{\partial \xi^k}{\partial T_{WJ}^k}\right)^2 u_c(T_{WJ}^k)^2 + \left(\frac{\partial \xi^k}{\partial T_{WJ+EWC}^k}\right)^2 u_c(T_{WJ+EWC}^k)^2 \\[2mm]
& + \left(\frac{\partial \xi^k}{\partial T_{fluid,WJ}}\right)^2 u_c(T_{fluid,WJ})^2
\end{aligned}
\qquad (49)
$$

Where: $u_c(T_{WJ}^k)$ and $u_c(T_{WJ+EWC}^k)$ are the combined uncertainty of T_{WJ}^k and T_{WJ+EWC}^k, respectively, following the same definition as $u_c(\overline{T^k})$. $u_c(T_{fluid,WJ})$ is the combined uncertainty of $T_{fluid,WJ}$, following the same definition as $u_c(\overline{T_i^k})$.

After partial derivatives computation, we obtain the final expression for $u_c(\xi^k)$ given in equation (50):

$$u_c(\xi^k) = \left(\frac{1}{\left(T_{WJ}^k - T_{fuid,WJ}\right)^2} u_c\left(T_{WJ}^k\right)^2 \right.$$

$$+ \frac{\left(T_{WJ+EWC}^k - T_{fuid,WJ}\right)^2}{\left(T_{WJ}^k - T_{fuid,WJ}\right)^4} u_c\left(T_{WJ+EWC}^k\right)^2 \qquad (50)$$

$$\left. + \frac{\left(T_{WJ+EWC}^k - T_{WJ}\right)^2}{\left(T_{WJ}^k - T_{fuid,WJ}\right)^4} u_c\left(T_{fluid,WJ}\right)^2 \right)^{1/2}$$

Eventually, the extended uncertainty $U_c(\xi^k)$ can be expressed following the same definition as in equation (48):

$$U_c(\xi^k) = k_{cov} \times u_c(\xi^k) \qquad (51)$$

A.3   Heat balance uncertainty

The final expression for the heat absorbed by the fluid, q_{fluid}, is given in (51). From this expression we can deduce the combined uncertainty $u_c(q_{fluid})$ as follows:

$$u_c(q_{fluid})^2 = \left(\frac{\partial q}{\partial \dot{V}}\right)^2 u_c(\dot{V})^2 + \left(\frac{\partial q_{fluid}}{\partial T_{inlet}}\right)^2 u_c(T_{inlet})^2$$

$$+ \left(\frac{\partial q_{fluid}}{\partial T_{outlet}}\right)^2 u_c(T_{outlet})^2 \qquad (52)$$

After partial derivatives computation and a few manipulations, we obtain the following expression for $u_c(q_{fluid})$:

$$u_c(q_{fluid})$$

$$= \rho_{fluid} c_{p_{fluid}} \sqrt{(T_{inlet} - T_{outlet})^2 u_c(\dot{V})^2 + \dot{V}^2 (u_c(T_{inlet})^2 + u_c(T_{inlet})^2)} \qquad (53)$$

Eventually, the extended uncertainty $U_c(\xi^k)$ can be expressed following the same definition as in equation (48):

$$U_c(q_{fluid}) = k_{cov} \times u_c(q_{fluid}) \qquad (54)$$

APPENDIX B.   WATER ETHYLENE GLYCOL

PROPERTIES

The density, specific heat, thermal conductivity and viscosity of WEG (50-50% mixture by volume of water and ethylene glycol) are given as a function of temperature in Figure 48. The experimental data is taken from [65], and the box for each graph corresponds to a polynomial regression of this experimental data.

(a) Density graph — $y = -2.18138E-03x^2 - 3.71197E-01x + 1.08166E+03$, $R^2 = 9.99654E-01$

(b) Specific Heat graph — $y = -1.47422E-06x^2 + 4.00925E-03x + 3.19625E+00$, $R^2 = 9.99575E-01$

(c) Thermal Conductivity graph — $y = -3.43435E-06x^2 + 8.01068E-04x + 3.53189E-01$, $R^2 = 9.98582E-01$

(d) Viscosity graph — $y = 2.610E-08x^4 - 1.247E-05x^3 + 2.245E-03x^2 - 1.901E-01x + 7.149E+00$, $R^2 = 1.000E+00$
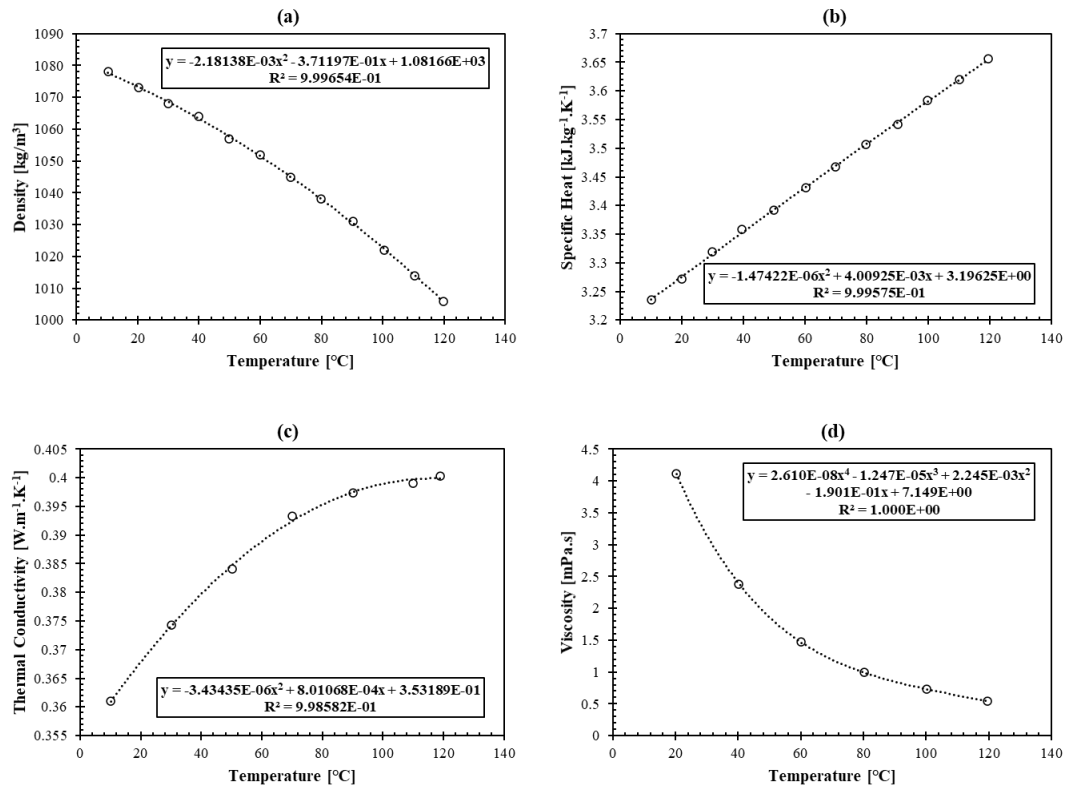
Figure 48 – Density (a), specific heat (b), thermal conductivity (c) and viscosity (d) of WEG (50-50% mixture by volume of water and ethylene glycol) with respect to temperature from 20°C to 120°C [65]

REFERENCES

[1]   I. E. A. (IEA), "Global EV Outlook 2019," IEA, Paris, 2019.

[2]   "Electrical and Electronics Technical Team Roadmap," U.S. Driving Research and Innovation for Vehicle efficiency and Energy sustainability, 2017.

[3]   D. Staton, A. Boglietti, and A. Cavagnino, "Solving the more difficult aspects of electric motor thermal analysis in small and medium size industrial induction motors," *IEEE Transactions on Energy Conversion,* vol. 20, no. 3, pp. 620-628, 2005, doi: 10.1109/TEC.2005.847979.

[4]   O. Bilgin and F. A. Kazan, "The effect of magnet temperature on speed, current and torque in PMSMs," in *2016 XXII International Conference on Electrical Machines (ICEM)*, 4-7 Sept. 2016 2016, pp. 2080-2085, doi: 10.1109/ICELMACH.2016.7732809.

[5]   A. A. Adly and A. Huzayyin, "The impact of demagnetization on the feasibility of permanent magnet synchronous motors in industry applications," *Journal of Advanced Research,* vol. 17, pp. 103-108, 2019/05/01/ 2019, doi: https://doi.org/10.1016/j.jare.2019.02.002.

[6]   C. Sciascera, M. Galea, P. Giangrande, and C. Gerada, "Lifetime consumption and degradation analysis of the winding insulation of electrical machines," in *8th IET International Conference on Power Electronics, Machines and Drives (PEMD 2016)*, 19-21 April 2016 2016, pp. 1-5, doi: 10.1049/cp.2016.0231.

[7]   Q. Chen, Z. Zou, and B. Cao, "Lumped-parameter thermal network model and experimental research of interior pmsm for electric vehicle," *CES Transactions on Electrical Machines and Systems,* vol. 1, no. 4, pp. 367-374, 2017, doi: 10.23919/TEMS.2017.8241358.

[8]   S. Mezani, N. Takorabet, and B. Laporte, "A combined electromagnetic and thermal analysis of induction motors," *IEEE Trans. Magn.,* vol. 41, no. 5, pp. 1572-1575, 2005, doi: 10.1109/TMAG.2005.845044.

[9]   D. A. Staton and A. Cavagnino, "Convection Heat Transfer and Flow Calculations Suitable for Electric Machines Thermal Models," *IEEE Transactions on Industrial Electronics,* vol. 55, no. 10, pp. 3509-3516, 2008, doi: 10.1109/TIE.2008.922604.

[10]   X. Yang, A. Fatemi, T. Nehl, L. Hao, W. Zeng, and S. Parrish, "Comparative Study of Three Stator Cooling Jackets for Electric Machine of Mild Hybrid Vehicle," in *2019 IEEE International Electric Machines & Drives Conference (IEMDC)*, 12-15 May 2019 2019, pp. 1202-1209, doi: 10.1109/IEMDC.2019.8785138.

[11]   M. Popescu, D. A. Staton, A. Boglietti, A. Cavagnino, D. Hawkins, and J. Goss, "Modern Heat Extraction Systems for Power Traction Machines—A Review," *IEEE Transactions on Industry Applications,* vol. 52, no. 3, pp. 2167-2175, 2016, doi: 10.1109/TIA.2016.2518132.

[12]   L. Mingda, L. Yingjie, D. Hao, and B. Sarlioglu, "Thermal management and cooling of windings in electrical machines for electric vehicle and traction application," in *2017 IEEE Transportation Electrification Conference and Expo (ITEC)*, 22-24 June 2017 2017, pp. 668-673, doi: 10.1109/ITEC.2017.7993349.

[13]   A. Boglietti, A. Cavagnino, and D. Staton, "Determination of Critical Parameters in Electrical Machine Thermal Models," *IEEE Transactions on Industry Applications,* vol. 44, no. 4, pp. 1150-1159, 2008, doi: 10.1109/TIA.2008.926233.

[14]   W. Sixel, M. Liu, G. Nellis, and B. Sarlioglu, "Ceramic 3D Printed Direct Winding Heat Exchangers for Improving Electric Machine Thermal Management," in *2019 IEEE Energy Conversion Congress and Exposition (ECCE)*, 29 Sept.-3 Oct. 2019 2019, pp. 769-776, doi: 10.1109/ECCE.2019.8913234.

[15]   S. A. Semidey and J. R. Mayor, "Experimentation of an Electric Machine Technology Demonstrator Incorporating Direct Winding Heat Exchangers," *IEEE Transactions on Industrial Electronics,* vol. 61, no. 10, pp. 5771-5778, 2014, doi: 10.1109/TIE.2014.2303779.

[16]   M. Diana, J. Colussi, A. L. Ganga, and P. Guglielmi, "An innovative slot cooling for integrated electric drives," in *2019 IEEE Workshop on Electrical Machines Design, Control and Diagnosis (WEMDCD)*, 22-23 April 2019 2019, vol. 1, pp. 191-196, doi: 10.1109/WEMDCD.2019.8887786.

[17]   C. Liu *et al.*, "Experimental Investigation on Oil Spray Cooling With Hairpin Windings," *IEEE Transactions on Industrial Electronics,* vol. 67, no. 9, pp. 7343-7353, 2020, doi: 10.1109/tie.2019.2942563.

[18]   B. Kekelia *et al.*, "Surface Temperature Effect on Convective Heat Transfer Coefficients for Jet Impingement Cooling of Electric Machines With Automatic Transmission Fluid," in *ASME 2019 International Technical Conference and Exhibition on Packaging and Integration of Electronic and Photonic Microsystems*, 2019, vol. ASME 2019 International Technical Conference and Exhibition on Packaging and Integration of Electronic and Photonic Microsystems, V001T08A004, doi: 10.1115/ipack2019-6457. [Online]. Available: https://doi.org/10.1115/IPACK2019-6457

[19]   V. Madonna, A. Walker, P. Giangrande, G. Serra, C. Gerada, and M. Galea, "Improved Thermal Management and Analysis for Stator End-Windings of Electrical Machines," *IEEE Transactions on Industrial Electronics,* vol. 66, no. 7, pp. 5057-5069, 2019, doi: 10.1109/TIE.2018.2868288.

[20]   S. Nategh, A. Boglietti, D. Barber, Y. Liu, and R. Brammer, "Thermal and Manufacturing Aspects of Traction Motors Potting: A Deep Experimental Evaluation," *IEEE Transactions on Energy Conversion,* vol. 35, no. 2, pp. 1026-1035, 2020, doi: 10.1109/tec.2020.2966606.

[21]   H. Li, K. W. Klontz, V. E. Ferrell, and D. Barber, "Thermal Models and Electrical Machine Performance Improvement Using Encapsulation Material," *IEEE Transactions on Industry Applications,* vol. 53, no. 2, pp. 1063-1069, 2017, doi: 10.1109/tia.2016.2641396.

[22]   Y. Sato, S. Ishikawa, T. Okubo, M. Abe, and K. Tamai, "Development of High Response Motor and Inverter System for the Nissan LEAF Electric Vehicle," 2011. [Online]. Available: https://doi.org/10.4271/2011-01-0350.

[23]   P. Mellor, R. Wrobel, and N. Simpson, "AC losses in high frequency electrical machine windings formed from large section conductors," in *2014 IEEE Energy Conversion Congress and Exposition (ECCE)*, 14-18 Sept. 2014 2014, pp. 5563-5570, doi: 10.1109/ECCE.2014.6954163.

[24]   P. H. Mellor, R. Wrobel, and N. McNeill, "Investigation of Proximity Losses in a High Speed Brushless Permanent Magnet Motor," in *Conference Record of the 2006 IEEE Industry Applications Conference Forty-First IAS Annual Meeting*, 8-12 Oct. 2006 2006, vol. 3, pp. 1514-1518, doi: 10.1109/IAS.2006.256730.

[25]   R. Wrobel, D. E. Salt, A. Griffo, N. Simpson, and P. H. Mellor, "Derivation and Scaling of AC Copper Loss in Thermal Modeling of Electrical Machines," *IEEE Transactions on Industrial Electronics,* vol. 61, no. 8, pp. 4412-4420, 2014, doi: 10.1109/TIE.2013.2266088.

[26]   C. Yicheng and P. Pillay, "An improved formula for lamination core loss calculations in machines operating with high frequency and high flux density excitation," in *Conference Record of the 2002 IEEE Industry Applications Conference. 37th IAS Annual Meeting (Cat. No.02CH37344)*, 13-18 Oct. 2002 2002, vol. 2, pp. 759-766 vol.2, doi: 10.1109/IAS.2002.1042645.

[27]   G. Bertotti, "General properties of power losses in soft ferromagnetic materials," *IEEE Trans. Magn.,* vol. 24, no. 1, pp. 621-630, 1988, doi: 10.1109/20.43994.

[28]   J. Chen, D. Wang, S. Cheng, Y. Wang, Y. Zhu, and Q. Liu, "Modeling of Temperature Effects on Magnetic Property of Nonoriented Silicon Steel Lamination," *IEEE Trans. Magn.,* vol. 51, no. 11, pp. 1-4, 2015, doi: 10.1109/TMAG.2015.2432081.

[29]   T. L. Mthombeni and P. Pillay, "Physical Basis for the Variation of Lamination Core Loss Coefficients as a Function of Frequency and Flux Density," in *IECON 2006 - 32nd Annual Conference on IEEE Industrial Electronics*, 6-10 Nov. 2006 2006, pp. 1381-1387, doi: 10.1109/IECON.2006.347545.

[30]   P. H. Mellor, D. Roberts, and D. R. Turner, "Lumped parameter thermal model for electrical machines of TEFC design," *IEE PROCEEDINGS-B,* vol. 138, no. 5, pp. 205 - 218, 1991, doi: 10.1049/ip-b.1991.0025.

[31]   J. Dong, Y. Huang, L. Jin, H. Lin, and H. Yang, "Thermal Optimization of a High-Speed Permanent Magnet Motor," *IEEE Trans. Magn.,* vol. 50, no. 2, pp. 749-752, 2014, doi: 10.1109/TMAG.2013.2285017.

[32]   W. Jiang and T. M. Jahns, "Development of efficient electromagnetic-thermal coupled model of electric machines based on finite element analysis," in *2013 International Electric Machines & Drives Conference*, 12-15 May 2013 2013, pp. 816-823, doi: 10.1109/IEMDC.2013.6556187.

[33]   W. Jiang and T. M. Jahns, "Coupled Electromagnetic–Thermal Analysis of Electric Machines Including Transient Operation Based on Finite-Element Techniques," *IEEE Transactions on Industry Applications,* vol. 51, no. 2, pp. 1880-1889, 2015, doi: 10.1109/TIA.2014.2345955.

[34]   P. K. Vong and D. Rodger, "Coupled electromagnetic-thermal modeling of electrical machines," *IEEE Trans. Magn.,* vol. 39, no. 3, pp. 1614-1617, 2003, doi: 10.1109/TMAG.2003.810420.

[35]   Y. Zhang, J. Ruan, T. Huang, X. Yang, H. Zhu, and G. Yang, "Calculation of Temperature Rise in Air-cooled Induction Motors Through 3-D Coupled Electromagnetic Fluid-Dynamical and Thermal Finite-Element Analysis," *IEEE Trans. Magn.,* vol. 48, no. 2, pp. 1047-1050, 2012, doi: 10.1109/TMAG.2011.2174433.

[36]   J. Nerg, M. Rilla, and J. Pyrhonen, "Thermal Analysis of Radial-Flux Electrical Machines With a High Power Density," *IEEE Transactions on Industrial Electronics,* vol. 55, no. 10, pp. 3543-3554, 2008, doi: 10.1109/TIE.2008.927403.

[37]   T. L. Bergman, A. S. Lavine, F. P. Incropera, and D. P. DeWitt, *Fundamentals of Heat and Mass Transfer*, 8th ed. United States of America: Wiley, 2017.

[38]   J. Mugglestone, S. J. Pickering, and D. Lampard, "Effect of geometric changes on the flow and heat transfer in the end region of a TEFC induction motor," in *1999. Ninth International Conference on Electrical Machines and Drives (Conf. Publ. No. 468)*, 3-1 Sept. 1999 1999, pp. 40-44, doi: 10.1049/cp:19990987.

[39]   D. Staton and S. Pickering, "Recent Advancement in the Thermal Design of Electric Motors," 2001.

[40]   A. Boglietti, A. Cavagnino, D. Staton, M. Shanel, M. Mueller, and C. Mejuto, "Evolution and Modern Approaches for Thermal Analysis of Electrical Machines," *IEEE Transactions on Industrial Electronics,* vol. 56, no. 3, pp. 871-882, 2009, doi: 10.1109/TIE.2008.2011622.

[41]   P. H. Mellor, D. Roberts, and D. R. Turner, "Lumped parameter thermal model for electrical machines of TEFC design," *IEE Proceedings B - Electric Power Applications,* vol. 138, no. 5, pp. 205-218, 1991, doi: 10.1049/ip-b.1991.0025.

[42]   A. M. E.-. Refaie, N. C. Harris, T. M. Jahns, and K. M. Rahman, "Thermal analysis of multibarrier interior PM synchronous Machine using lumped parameter model," *IEEE Transactions on Energy Conversion,* vol. 19, no. 2, pp. 303-309, 2004, doi: 10.1109/TEC.2004.827011.

[43]   S. Nategh, O. Wallmark, M. Leksell, and S. Zhao, "Thermal Analysis of a PMaSRM Using Partial FEA and Lumped Parameter Modeling," *IEEE Transactions on Energy Conversion,* vol. 27, no. 2, pp. 477-488, 2012, doi: 10.1109/TEC.2012.2188295.

[44]   J. Qi, W. Hua, and H. Zhang, "Thermal Analysis of Modular-Spoke-Type Permanent-Magnet Machines Based on Thermal Network and FEA Method," *IEEE Trans. Magn.,* vol. 55, no. 7, pp. 1-5, 2019, doi: 10.1109/TMAG.2019.2905873.

[45]   N. Rostami, M. R. Feyzi, J. Pyrhonen, A. Parviainen, and M. Niemela, "Lumped-Parameter Thermal Model for Axial Flux Permanent Magnet Machines," *IEEE Trans. Magn.,* vol. 49, no. 3, pp. 1178-1184, 2013, doi: 10.1109/TMAG.2012.2210051.

[46]   H. Zhang *et al.*, "Thermal Model Approach to Multisector Three-Phase Electrical Machines," *IEEE Transactions on Industrial Electronics,* vol. PP, pp. 1-1, 03/06 2020, doi: 10.1109/TIE.2020.2977559.

[47]   A. Boglietti, A. Cavagnino, and D. A. Staton, "TEFC induction motors thermal models: a parameter sensitivity analysis," in *Conference Record of the 2004 IEEE Industry Applications Conference, 2004. 39th IAS Annual Meeting.*, 3-7 Oct. 2004 2004, vol. 4, pp. 2469-2476 vol.4, doi: 10.1109/IAS.2004.1348822. [Online]. Available: https://ieeexplore.ieee.org/document/1348822/

[48]   R. Wrobel and P. H. Mellor, "A General Cuboidal Element for Three-Dimensional Thermal Modelling," *IEEE Trans. Magn.,* vol. 46, no. 8, pp. 3197-3200, 2010, doi: 10.1109/TMAG.2010.2043928.

[49]   G. Moreno, "Thermal Performance Benchmarking: Annual Report,"; National Renewable Energy Lab. (NREL), Golden, CO (United States), NREL/MP-5400-64941 United States 10.2172/1247461 NREL English, 2016. [Online]. Available: https://www.osti.gov/servlets/purl/1247461

[50]   J. E. Cousineau, K. Bennion, D. DeVoto, and S. Narumanchi, "Experimental characterization and modeling of thermal resistance of electric machine lamination stacks," *International Journal of Heat and Mass Transfer,* vol. 129, pp. 152-159, 2019/02/01/ 2019, doi: https://doi.org/10.1016/j.ijheatmasstransfer.2018.09.051.

[51] J. Emily Cousineau, K. Bennion, V. Chieduko, R. Lall, and A. Gilbert, "Experimental Characterization and Modeling of Thermal Contact Resistance of Electric Machine Stator-to-Cooling Jacket Interface Under Interference Fit Loading," *Journal of Thermal Science and Engineering Applications,* vol. 10, no. 4, 2018, doi: 10.1115/1.4039459.

[52] A. A. Wereszczak *et al.*, "Anisotropic Thermal Response of Packed Copper Wire," *Journal of Thermal Science and Engineering Applications,* vol. 9, no. 4, 2017, doi: 10.1115/1.4035972.

[53] "Modelling the Nissan Leaf Motor using Motor-CAD," Motor Design Ltd., 2019. [Online]. Available: https://www.motor-design.com/publications/tutorials/

[54] R. Wrobel, S. J. Williamson, J. D. Booker, and P. H. Mellor, "Characterizing the in situ Thermal Behavior of Selected Electrical Machine Insulation and Impregnation Materials," *IEEE Transactions on Industry Applications,* vol. 52, no. 6, pp. 4678-4687, 2016, doi: 10.1109/tia.2016.2589219.

[55] K. Bennion and J. Cousineau, "Sensitivity analysis of traction drive motor cooling," in *2012 IEEE Transportation Electrification Conference and Expo (ITEC)*, 18-20 June 2012 2012, pp. 1-6, doi: 10.1109/ITEC.2012.6243512. [Online]. Available: https://ieeexplore.ieee.org/document/6243512/

[56] "Comparison of Sealing Methods for FDM Materials," in "Technical Application Guide," Stratasys Inc., Technical Application Guide 2014.

[57] P. H. Corporation, *Parker O-Ring Handbook* (ORD 5700). Cleveland, OH, 2018, p. 292.

[58] M. Fischer and V. Schöppner, "Some Investigations Regarding the Surface Treatment of Ultem * 9085 Parts Manufactured with Fused Deposition Modeling," 2013.

[59] P. S. Srinivasan, S. S. Nandapurkar, and F. A. Holland, "Friction Factors for Coils," *Trans. Inst. Chem. Eng.,* vol. 48, pp. T156-T161, 1970.

[60] F. R. Menter, "Two-equation eddy-viscosity turbulence models for engineering applications," *AIAA J.,* vol. 32, no. 8, pp. 1598-1605, 1994, doi: 10.2514/3.12149.

[61] M. Stegelmann, M. Müller, A. Winkler, A. Liebsch, and N. Modler, "Polymer Analyses for an Adapted Process Design of the Pipe-Extrusion of Polyetherimide," *Materials Sciences and Applications,* vol. 9, pp. 614-624, 2018, doi: 10.4236/msa.2018.97044.

[62] J. Godbehere, R. Wrobel, D. Drury, and P. H. Mellor, "Experimentally calibrated thermal stator modelling of AC machines for short-duty transient operation," in *2016 XXII International Conference on Electrical Machines (ICEM)*, 4-7 Sept. 2016 2016, pp. 1721-1727, doi: 10.1109/ICELMACH.2016.7732756.

[63]   *Measurement Uncertainty Analysis Principles and Methods, NASA Measurement Quality Assurance Handbook - ANNEX 3*, NASA-HDBK-8739.19-3, N. A. a. S. Administration, Washington DC, 2010.

[64]   *Evaluation of measurement data - Guide to the expression of uncertainty in measurement*, JCGM 100, JCGM, 2008.

[65]   "2009 ASHRAE Handbook - Fundamentals," SI Edition ed: American Society of Heating, Refrigerating and Air-Conditioning Engineers, Inc. (ASHRAE), 2009.